Soft-sphere simulations of a planar shock interaction with a granular bed

Cameron Stewart, S. Balachandar, and Thomas P. McGrath

Phys. Rev. Fluids **3**, 034308 — Published 26 March 2018

DOI: 10.1103/PhysRevFluids.3.034308

Soft-sphere simulations of a planar shock interaction with a granular bed

Cameron Stewart, S. Balachandar, Thomas P. McGrath
University of Florida, University of Florida, NSWC IHEODTD
(Dated: March 4, 2018)

Here we consider the problem of shock propagation through a layer of spherical particles. A point particle force model is used to capture the shock-induced aerodynamic force acting upon the particles. The discrete element method (DEM) code LIGGGHTS is used to implement the shock-induced force as well as to capture the collisional forces within the system. A volume fraction dependent drag correction is applied using Voronoi tessellation to calculate the volume of fluid around each individual particle. A statistically stationary frame is chosen so that spatial and temporal averaging can be performed to calculate ensemble-averaged macroscopic quantities, such as the granular temperature. A parametric study is carried out by varying the coefficient of restitution for three sets of multiphase shock conditions. A self-similar profile is obtained for the granular temperature that is dependent on the coefficient of restitution. A traveling wave structure is observed in the particle concentration downstream of the shock and this instability arises from the volume fraction dependent drag force. The intensity of the traveling wave increases significantly as inelastic collisions are introduced. Downstream of the shock, the variance in Voronoi volume fraction is shown to have a strong dependence upon the coefficient of restitution, indicating clustering of particles induced by collisional dissipation. Statistics of the Voronoi volume are computed upstream and downstream of the shock and compared to theoretical results for randomly distributed hard-spheres.

I. INTRODUCTION

Shock propagation through a particle-laden medium is an important process that has many technological and environmental applications. Explosive volcanic eruption and supernova are spectacular examples of shock propagation through a multiphase medium in nature. Multiphase shock propagation is fundamental to understanding, characterizing, and predicting the effect of heterogeneous explosives. Modern heterogeneous explosives include metal particles within the explosive material. Upon detonation, the explosive material is converted into a hot dense gas which rapidly expands. Particles packed within the explosive are compressed and accelerated by the passing shock wave, and begin to radially disperse. Other engineering applications include shock-induced dispersion of particles and droplets, as well as accidental explosions in mines and grain silos. In all these examples it is critically important to understand the dynamics of the particles within the early period of interaction with the shock, since this interaction between the particles and the surrounding gas has the potential to nucleate instabilities, which in turn affect the long-time evolution of the system.

A multiphase flow model of shock propagation over a particle-laden gas should account for the two-way coupling between the gas and the particles. The forward coupling accounts for the influence of the shock and the post-shock gas flow on the particles. The dispersed particles generate reflected waves that travel upstream into the gas and forms a transmitted shock that travels through the particle-laden gas. The transmitted shock strength deviates from that of the incident shock depending on the strength of the reverse coupling of particles on the flow. At very dilute particle volume fractions, a two-way coupled description is sufficient since particle-particle interactions are negligible. However, as particle volume fraction increases, the effect of indirect interactions between the particles, mediated by the surrounding gas, becomes important and must be taken into account through drag force modification [10]. With further increases in particle volume fraction, the multiphase flow enters the four-way coupled regime [14], whereby collisions between the particles become important to the overall momentum and energy balance. This regime can be termed the *collisional regime*. As the particle volume fraction further increases and approaches the close-packing limit, the physics of shock propagation through the particle-laden medium is significantly controlled by the enduring contacts between the particles (*compaction regime*). In this regime, the momentum balance is dominantly controlled by the contact forces between the particles. This work focuses on the collisional regime where the particle-particle interactions play an important role.

While applications often require descriptions of shock propagation in multi-phase materials in complex geometries, understanding multi-phase shock propagation even in simple planar geometry remains a formidable problem and is still under active study. Rogue et al. [35] performed experiments to investigate the interaction of a strong planar shock wave with a horizontal bed of particles within a vertical shock-tube. Recent work by Wagner et al. [48] considered a horizontal shock-tube where a vertical curtain of particles is subjected to a strong planar shock wave. These shock tube experiments have provided valuable information about the macroscopic effect (behavior) of the propagating shock on the particle phase (e.g. downstream evolution of the location of the head and tail of the particle curtain). However, the detailed physics occurring at the microscale remains inaccessible in these experiments due to the inability to measure the effect of particle-particle interactions. Such interactions come about through direct collisional interactions and through indirect interactions such as neighbor-induced drag force modulation [2, 4, 6, 45, 46, 50]. Understanding these particle-particle interactions is crucial to developing models for shock-particle interaction at intermediate particle volume fractions, and this motivates our current study. Goldshtein et al. [20] studied the problem of planar shock propagation through a single-phase granular medium driven by a piston rapidly moving into a quiescent medium. Using granular kinetic theory, the Eulerian hydrodynamic equations were solved to obtain a closed-form self-similar solution for the granular medium within a fluidized region ahead of the piston.

We consider a similar problem, where a quiescent particle-laden medium is subjected to an incoming planar shock wave. The Euler-Lagrange approach is used to investigate the shock propagation over a particle-laden medium at the microscale, which has an initially statistically uniform distribution of spherical particles. This simplified set up is one-dimensional, and is inhomogeneous only in the direction of shock propagation and is statistically homogeneous in the transverse directions. Furthermore, in the shock-attached frame of reference the problem is stationary, thus permitting averaging over time as well as over the homogeneous transverse directions. The gas phase is treated as a continuum and averaged within a reference volume element, while discrete particles are tracked in the Lagrangian frame. A point particle model is used for computing the time-dependent force on each particle as the shock propagates over it [24, 25, 32, 33]. The collective effect neighbors have on the drag force acting upon each particle is taken into account in terms of the local Voronoi volume fraction dependent drag [49]. A soft-sphere discrete element method (DEM) is used to simulate particle-particle collisions with a spring dash-pot force model. Through DEM simulations, we capture the collision-induced internal stresses within the particle phase.

DEM simulations have been extensively applied in the study of 1-D stationary granular shear flows [9, 21, 47], and have been very valuable in understanding the collisional physics and in the calibration of kinetic theory based closure models [9, 18, 21, 47]. Study of the planar shock propagation over a particle bed complements the granular shear flow problem in several ways. The shear flow problem can be made both homogeneous and stationary with periodic boundary conditions along all three directions. If the granular shear flow is confined between two parallel plates, then the problem is inhomogeneous in the wall normal direction. However, the region of inhomogeneity is typically limited to thin layers close to the bounding plates; the majority of the domain away from the bounding plates can be considered homogeneous. In comparison, the problem of planar shock propagation over a particle bed is strongly inhomogeneous in the streamwise direction. This complicates the analysis since the statistical results are now dependent on the inhomogeneous direction. The granular shear flow is driven by gravity and the effect of surrounding fluid is often ignored. In our current study, the particles are driven by the shock and the post-shock gas flow. This introduces the need for a point particle model for the force exerted by the gas on the particles.

The macroscale behavior of shock propagation through a particle-laden fluid has been addressed by Rudinger [37, 38]. He defined the following three regions: (i) Immediately downstream of the multiphase shock is the frozen region where the particle properties are the same as those of the gas-particle equilibrium mixture upstream of the shock. (ii) Sufficiently downstream of the shock the gas-particle mixture is in equilibrium corresponding to the terminal post-shock condition. (iii) The relaxation region where the mixture is not in equilibrium, since both the particle and gas phases are evolving from their pre- to post-shock states. Rudinger [37, 38] accounted for the two-way coupling between the particles and the gas at the macroscale, and provided shock relations for the downstream equilibrium regime. The particles' influence on the shock can be separated into a macroscale influence and a microscale influence. At the macroscale, since the flow has been averaged over the reference volume, the shock as well as the post-shock flow will remain planar.

At the microscale, the shock propagation around the randomly distributed particles becomes quite complicated due to multitudes of wave reflections and diffractions. The point particle force model to be employed in the present work is based on undisturbed flow approaching the particle. Therefore it is sufficient to know the details of the propagating shock at the macroscale in order to evaluate the forces on the individual particles. Information on the influence of the neighboring particles is taken into account through the Voronoi volume of each particle. This approach is consistent with previous implementations of multiphase DEM [11]. We further simplify the problem by assuming that the gas properties transition from the pre- to post-shock equilibrium states entirely across the shock. Thus, only the particle properties are allowed to evolve in the relaxation region.

The simplifications allow us to focus on the process by which a random distribution of particles, in equilibrium before the arrival of the shock, approaches its new post-shock equilibrium state. We consider the finite volume fraction regime where both the gas-mediated particle-particle interaction and direct collision between the particles are important. It is known in the fluidized-bed literature that volume fraction dependence of drag can lead to instabilities in the particle distribution [13, 30]. Such instabilities are observed in the present shock driven particle-laden flows as well, resulting in clustering of particles in the post-shock regime. The structure and tendencies of the clustering are investigated, as well as the effect of collisional parameters on the clustering. Voronoi volume statistics [17, 29, 39] are used to quantify the nature and amount of particle clustering downstream of the shock and results are compared with an analytical 3Γ distribution [41].

The rest of the paper is arranged as follows. In Section II we present the details of the discrete element simulations, particle collision model, and the point particle force model. Force fluctuations are introduced using a Voronoi tessellation based volume fraction in conjunction with an empirical drag correction. Details of multiphase shock relations are presented. Data processing methods are presented in Section III. Section IV discusses the results from three different cases with varied multiphase shock properties. For each case, a parametric study is carried out by varying the coefficient of restitution. A traveling wave-like structure is observed in the particle concentration downstream of the shock, which is studied by investigating the Voronoi volume fraction statistics both upstream and downstream of the shock, and comparing the results to Voronoi statistics for randomly distributed particles. The coefficient of restitution is shown to have a significant impact upon the Voronoi volume statistics downstream of the shock, indicating that inelastic collisions lead to a clustered micro-structure within the particle bed. The granular temperature as calculated directly from the DEM results are presented and discussed. Section V provides a summary of the results and discusses future work.

II. NUMERICAL APPROACH

Our interest is to study the collisional dynamics that arises from the propagation of a planar shock wave through a bed of particles. Therefore the volume fraction of particles within the bed is chosen to be at intermediate values ranging from about $\phi = 0.05$ to $\phi = 0.55$, so that particle-particle collisions are frequent and important in the overall momentum balance. The discrete element method code LIGGGHTS has been modified to implement the numerical method presented below, and to carry out the simulations.

A. Problem Setup

We consider a computational domain that is stationary in a shock-attached reference frame where the x-direction is the direction of shock propagation (see Figure 1). In the lab reference frame, the pre-shock gas and particle distributions are fixed. In the shock-attached frame, the pre-shock gas and particles approach the shock at the shock velocity. As the gas passes through the shock, it rapidly slows and is compressed to its post-shock state. The particles first go through a rapid deceleration due to the inviscid forces that act on the acoustic time scale, followed by a slower deceleration due to the viscous forces, and finally approach the post-shock gas velocity. Correspondingly, the particle volume fraction increases substantially from the initial value after passing through the shock. In the shock-attached frame, the pre-shock state is taken as upstream and extends in the negative x-direction, and the post-shock state is taken as downstream and extends in the positive x-direction.

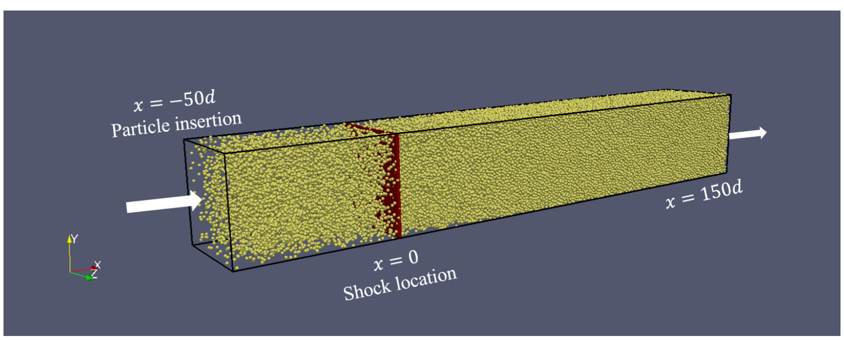

FIG. 1: Representative simulation setup in the shock-attached frame of reference: Randomly packed particles enter on the left hand side at the laboratory shock speed. At $x = 0$ they encounter a planar shock and experience a shock modulated force causing collisions.

For the simulation cases discussed in this paper, we use two different domain sizes. Dimensions of the computational domain scale to accommodate the inertial relaxation of the particles towards the equilibrium state. In other words, the length downstream of shock is chosen such that the particles will decelerate and attain the post-shock gas velocity before exiting the domain. This relaxation length depends on both the particle size and the particle-to-gas density ratio. For Case 1, we extend the domain $150d$ downstream of the shock, where d denotes the particle diameter. Cases 2 and 3 extend $500d$ downstream of the shock. For all three cases, the computational domain extends $50d$

upstream of the shock, with a stationary planar shock located at $x = 0$. In the y and z-directions, the computational domain extends from $-15d$ to $+15d$. Periodic boundary conditions are employed along the y and z-directions. Therefore, the domain size along these directions is chosen to be larger than the correlation lengths, but small enough that the number of particles to be simulated is manageable. Thus, our simulation domain has a total size of $200d \times 30d \times 30d$ for Case 1, and a total size of $550d \times 30d \times 30d$ for Cases 2 and 3.

Inflow and outflow conditions in the streamwise direction are used at the $-x$ and $+x$ boundaries, respectively. The choice of a shock-attached reference frame makes the problem statistically stationary, and the incoming particles enter the computational domain at a uniform speed equal to the shock-speed in the laboratory frame. Due to downstream advection of particles, new particles must be constantly inserted at the inflow plane every time-step to retain the initial volume fraction ϕ_0. Particles leaving the domain in the x-direction are deleted.

A number of particle and gas related parameters are of importance in the present problem. Particle parameters such as density, diameter, Young's modulus, Poisson ratio, and the normal coefficient of restitution dictate the behavior of individual particle-particle collisions, while volume fraction dictates the number of collisions. Similarly, the rate of momentum exchange between the particles and the gas depends on shock strength and parameters such as particle diameter and particle-to-gas density ratio. In the first set of simulations to be discussed below we vary the coefficient of restitution, while holding the shock properties and particle-to-gas density ratio fixed. Additional sets of simulations will be reported where we vary the shock properties to investigate their influence. Tables I and II below present the particle and fluid properties employed in our simulations. The particle properties are chosen to be representative of aluminum and the gas is modeled as a very dense ideal gas.

TABLE I: Particle properties

Diameter: d	$100\,\mu m$
Young's modulus: Y	$70\,GPa$
Poisson ratio: μ	0.35
Density: ρ_p	$2.7\,g/cc$
Normal coefficient of restitution: e	$0.4 - 1$

TABLE II: Gas properties

Gas viscosity : ν_g	$0.05\,cm^2/s$
Particle-Gas density ratio (pre-shock): $\frac{\rho_p}{\rho_0}$	100
Speed of sound (pre-shock): a_0	$34311\,cm/s$
Specific heat ratio: γ	1.4

In the following subsections we will present (i) the multiphase flow shock relations that yield the gas properties upstream and downstream of the shock, (ii) the equations of motion that control the evolution of the particle, (iii) the aerodynamic force model, and (iv) the soft-sphere collision model, which collectively is the complete numerical methodology implemented in LIGGGHTS.

B. Multiphase Shock Relations

We first define the pre- and post-shock states of the particle-laden gas flow. For a normal shock wave traveling through an ideal gas, the standard Rankine-Huguenot conditions apply. These jump conditions must be appropriately modified in the case of a shock propagating through a particle-laden gas, as the presence of the particle phase alters the overall mass, momentum and energy balances across the shock. Furthermore, the effective thermodynamic properties of the gas-particle mixture are different from those of the pure gas.

In the case of shock propagation through a particle-laden gas, there are three distinct regions that can be identified in the post-shock state. The first is the frozen region directly behind the shock, where there is an instantaneous jump in the gas properties. Due to inertia, the particles do not rapidly change from their initial properties across the shock. This instantly generates a slip between the particle phase and the post-shock gas velocity, and a difference between the gas and particle temperatures. The frozen region is followed by the non-equilibrium region (or relaxation regime), where both the particle phase properties and the post-shock gas properties evolve towards an equilibrium. If the coupling to the gas phase is weak, then the change in the gas properties across the relaxation regime is much smaller than the change in the particle properties. Lastly, an equilibrium region is observed where the particle and gas phase properties have reached equilibrium. Carrier [8] considered the "dusty-gas" approximation of multiphase shock in the limit when the particle volume fraction is negligible. Carrier's dusty gas approximation was advanced in the works by Rudinger [37, 38], who described properties of the relaxation regime in the dilute limit and later discussed the frozen and equilibrium regimes for finite volume fractions.

Using the thermodynamic properties of the mixture, the balance equations for the gas and particle phases can be solved for the equilibrium state values. In the following discussion, the subscript 0 refers to the incoming pre-shock flow in the shock-attached frame of reference, while the subscript e corresponds to the final equilibrium state. In this shock-attached frame, the pre-shock gas velocity u_0 is the lab frame shock velocity and therefore the shock Mach number is given by $M_S = u_0/\alpha_0$. The pre-shock mixture speed of sound α_0 depends on the ratio of specific heats for the gas-particle mixture defined as

$$\gamma_{mix,0} = \gamma \frac{1+\delta\eta_0}{1+\gamma\delta\eta_0}, \tag{1}$$

where γ is the specific heat ratio of the pure gas. Here $\delta = c/c_p$ is the ratio of particle specific heat c to the specific heat at constant pressure of the gas c_p. The mass loading parameter is defined as

$$\eta_0 = \frac{\rho_p}{\rho_{g0}} \frac{\phi_0}{1-\phi_0}, \tag{2}$$

where ρ_p and ρ_{g0} are the particle and pre-shock gas densities, and ϕ_0 is the initial pre-shock particle volume fraction. Note that the definitions of specific heat ratio and mass loading are for the pre-shock state.

From the above definitions, the speed of sound within the particle-laden mixture at the pre-shock condition (α_0) can be expressed in terms of the speed of sound within the pure gas at the pre-shock state (a_0) as

$$\left(\frac{\alpha_0}{a_0}\right)^2 = \frac{\gamma_{mix,0}}{\gamma(1+\eta_0)(1-\phi_0)^2} = \frac{M_{g0}^2}{M_S^2}\,, \tag{3}$$

where $M_{g0} = u_0/a_0$ is the pure gas shock Mach number. An important characteristic of (3) is that as $\phi_0 \to 0$, $\alpha \to a_0$, and in the dilute regime, increasing ϕ lowers the mixture sound speed. Thus, the mixture sound speed is lower than the gas sound speed, leading to supersonic mixture Mach numbers even at subsonic gas conditions. In the present work, we set $M_{g0} = 1$, which for $\phi_0 \neq 0$ will lead to a multiphase shock of finite strength. The multiphase shock Mach number is then given by (3). The ratio of equilibrium and pre-shock gas velocity, particle volume fraction, gas density, and gas pressure can be expressed in terms of known quantities as

$$\frac{u_e}{u_0} = \frac{(\gamma_{mix}-1)M_S^2 + 2 + 2\phi_0(M_S^2-1)}{(\gamma_{mix}-1)M_S^2} \tag{4}$$

$$\frac{\phi_e}{\phi_0} = \frac{u_0}{u_e} \tag{5}$$

$$\frac{\rho_e}{\rho_0} = \frac{1-\phi_e}{1-\phi_0}\frac{u_0}{u_e} \tag{6}$$

$$\frac{p_e}{p_0} = 1 + (1-\phi_0)\gamma(1+\eta)(1-\frac{u_e}{u_0})M_g^2. \tag{7}$$

We emphasize that in the present simulation we do not solve the compressible gas flow equations. For a given set of gas and particle properties upstream of the shock, the downstream equilibrium properties of gas are obtained from the above relationships. We assume a weak coupling to the gas phase while in the non-equilibrium region. Therefore, the gas properties do not relax but sharply jump from the upstream to the downstream equilibrium values across the shock. This results in the shock remaining planar and of constant shock strength as it propagates through the bed of particles at the macroscale. This assumption avoids the need for a compressible gas flow solver.

C. Particle Equations of Motion

While the gas properties undergo a sharp transition across the shock, the particle phase undergoes a smooth relaxation from the pre-shock equilibrium state to the final post-shock equilibrium state. The evolution of each particle is tracked by solving Newton's equations of motion, where the force acting on the ith particle $\boldsymbol{F}_i$ is broken down into two contributions, an inter-phase coupling force exerted by the gas upon the particle $\boldsymbol{F}_{gp,i}$, and an inter-particle force $\boldsymbol{F}_{pp,i}$ due to the collision between the ith particle with all its neighbors. The equations of motion for the particles are

$$m_p\frac{d\boldsymbol{v}_i}{dt} = \boldsymbol{F}_i = \boldsymbol{F}_{gp,i} + \boldsymbol{F}_{pp,i} \qquad \text{and} \qquad \frac{d\boldsymbol{x}_i}{dt} = \boldsymbol{v}_i\,, \tag{8}$$

where $\boldsymbol{x}_i$ and $\boldsymbol{v}_i$ are particle position and velocity respectively. We ignore the rotational motion of the particles, and as a result ignore the friction force between the particles during inter-particle collision, and the torque imparted on the particles during collision. We ignore the net aerodynamic torque on the particle as the shock propagates past the particle. Next we describe the aerodynamic force model for $\boldsymbol{F}_{gp,i}$ and the soft-sphere collision model for $\boldsymbol{F}_{pp,i}$.

D. Aerodynamic force: Point particle model

Since the gas properties are known from the multiphase shock relations, the aerodynamic force on each particle can be explicitly calculated in terms of its position, velocity and acceleration. However, it is not sufficient to only account for the quasi-steady drag force that arises from the relative velocity between the particle and the surrounding gas. In shock-particle interactions, forces due to the gas acceleration as well as the relative acceleration between the particle and the surrounding gas can be substantial and therefore must be included in the equation of particle motion [24, 25]. Following the works of Parmar et al. [33] and Annamalai & Balachandar [5], the non-dimensional force acting on a spherical particle in a compressible flow is given by the following point particle force model:

$$\boldsymbol{f}_{gp} = \boldsymbol{f}_{pg} + \boldsymbol{f}_{qs} + \boldsymbol{f}_{iu} + \boldsymbol{f}_{vu} \tag{9}$$

where the total gas-particle coupling force is expressed as a superposition of pressure gradient (pg), quasi-steady (qs), inviscid unsteady (iu), and viscous unsteady (vu) force contributions. Each of these forces can be expressed in terms of particle and the undisturbed gas flow properties, evaluated at the particle. Note that the shock thickness is typically much smaller than the particle size and thus as the shock passes over a particle, part of the particle is still upstream of the shock, while the rest of the particle is downstream of the shock. This complicates the evaluation of undisturbed gas flow properties at the particle location, as they cannot be simply taken to be their values at the particle center. As will be shown below, a generalization of the Faxén's theorem will be used, which employs gas properties that are averaged over the surface or volume of the particle, and thus can be well defined even as the gas properties sharply vary across the upstream and downstream portions of the particle.

1. *Pressure gradient force*

The pressure gradient force (also known as the Archimedes force) is the undisturbed flow force. In the absence of the particle, this is the force that is experienced by the volume of fluid that occupies the particle location. The other three force contributions arise due to the presence of the particle and the flow perturbations induced by the no-slip and no-penetration boundary conditions on the particle. The pressure gradient force can be expressed as

$$\boldsymbol{f}_{pg} = \frac{4}{3}\pi R^3 \overline{\rho_g \frac{D\boldsymbol{u}}{Dt}}^V , \tag{10}$$

where $D\boldsymbol{u}/Dt$ is the total acceleration of the undisturbed fluid (i.e., total gas acceleration in the absence of the particle), ρ_g is the gas density and R is the particle radius. Here $\overline{()}^V$ indicates an average over the volume occupied by the particle. The undisturbed flow is taken to be governed by the inviscid Euler equation and thus the effects of viscous stresses in the undisturbed flow are ignored. Omitting the volume averaging and simply using $[\rho_g D\boldsymbol{u}/Dt]$ evaluated at the particle center, the pressure gradient force would be equivalent to a delta function that generates a non-zero impulse only at the time when the shock cross the particle center. In contrast, the Faxén form given in (10) predicts a finite pressure gradient force that remains non-zero, as long as the undisturbed shock is located somewhere over the particle. The importance of this generalization will become clear in section II D 5 where we validate the model.

2. *Quasi-steady force*

The quasi-steady force depends only on the instantaneous relative velocity between the particle and the fluid, and it is given by

$$\boldsymbol{f}_{qs} = 6\pi R \nu_g \overline{\rho_g(\boldsymbol{u}-\boldsymbol{v})}^S \Phi , \tag{11}$$

where ν_g is the kinematic viscosity of the fluid, which is taken to be constant. In the standard application of the point particle model, the undisturbed flow velocity at the particle, $\boldsymbol{u}$, will be evaluated at the center of the particle. For the quasi-steady force, an appropriate definition of undisturbed ambient flow velocity seen by the particle that fully accounts for the ambient flow variation was rigorously derived by Faxén [15] to be $\overline{\boldsymbol{u}}^S$, where the overbar with a superscript S indicates an average over the surface of the particle. The quasi-steady force expression given in (11) is a generalization of the Faxén's theorem to compressible flows, and it accounts for spatial variations in both density and velocity of the ambient gas flow on the scale of the particle. See Parmar et al. [33] and Annamalai & Balachandar [5] for a rigorous derivation of the above force expression from a solution of the linearized Navier-Stokes equations for compressible flow over a spherical particle.

In (11), Φ represents the correction to the quasi-steady force due to finite Reynolds number and finite volume fraction. The following empirical correction factor is employed here:

$$\Phi = \begin{cases} (1+0.15Re_i^{0.687})(1-\phi_{v,i})^{-3.7} & \text{if } Re_i < 1000 \\ (0.01833 Re_i)(1-\phi_{v,i})^{-3.7} & \text{if } Re_i \geq 1000 \, , \end{cases} \tag{12}$$

where $\phi_{v,i}$ is the local Voronoi volume fraction around the ith particle. The Reynolds number of the ith particle is defined in terms of the surface averaged relative velocity as

$$Re_i = \frac{2R\overline{|\boldsymbol{u} - \boldsymbol{v}|}^S}{\nu_g} \,. \tag{13}$$

The Reynolds number dependence in (12) is from Rowe [36], and the volume fraction correction is given by Wen and Yu [49].

The volume fraction dependence is of particular importance in the present simulation, since without dependence upon $\phi_{v,i}$, all particles at the same streamwise location will see the same undisturbed flow and therefore will experience the same streamwise force. In reality, however, the quasi-steady force will vary from particle to particle, and this force variation is due to the influence of the neighboring particles [28]. Due to the random distribution of particles, each particle sees a somewhat differently perturbed shock due to the spatial arrangement of its neighbors. The current model accounts for the gas-mediated influence of the neighboring particles through the local volume fraction-dependent correction. In the limit of $\phi_i \to 0$, the ith particle is far from all its neighbors and its quasi-steady force is that of an isolated particle. With increasing local volume fraction, according to the simple model of Wen and Yu [49], the effect of neighbors is an increase in drag force due to a crowding effect and acceleration of the flow between the particles. There are other models that account for the volume fraction effect on quasi-steady force [3, 34]; the key feature of all these models is to increase drag force with increasing volume fraction.

Voronoi tessellation

The local volume fraction associated with each particle is calculated using Voronoi tessellation. Voronoi tessellation takes a set of N particles in 3-D space and a containing bounding box, and divides the space into N Voronoi cells, each containing a single particle. The boundaries of a Voronoi cell are defined such that all points interior to the cell are closer to the particle center contained within the cell than any other particle. In other words, each bounding face of a Voronoi cell passes through the midpoint of the vector between the given particle and each of its nearest neighbors. In the present DEM simulation, a Voronoi tessellation can be accomplished at each time step using the N particle locations. Figure 2 shows a sample Voronoi tessellation from the present work where only edges of the Voronoi volumes around the particles are shown. From the volume of the Voronoi cell that encloses a particle, the local Voronoi volume fraction of that particle can be calculated as

$$\phi_{v,i}(t) = \frac{V_p}{V_i(t)} \,, \tag{14}$$

where V_p is the volume of the particle and $V_i(t)$ is the time-dependent volume of the Voronoi cell that encloses the ith particle. The open source C++ package VORO++ is used to carry out the Voronoi tessellation within the LIGGGHTS implementation. Periodic boundaries are used for the tessellation in the y and z-directions.

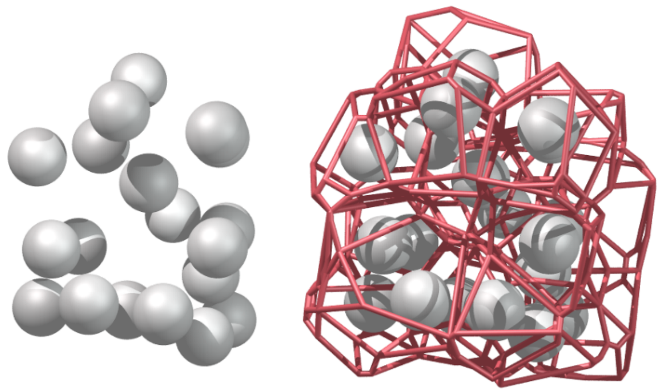

FIG. 2: (Left) A sample random distribution of particles. (Right) The particle distribution encapsulated by a Voronoi tessellation. The edges of the Voronoi cells are shown in red.

The particles are considered to be stationary in the lab frame before the arrival of the shock. In the shock-attached frame, this translates to particles being introduced at the inlet with a constant velocity. There is no gas-particle velocity difference nor particle-particle collisions upstream of the shock. In the post-shock regime, the variation in quasi-steady force plays an important role in introducing velocity fluctuation. This velocity fluctuation in turn is responsible for inter-particle collisions. Due to the highly nonlinear nature of the volume fraction dependent drag correction, small variations in local volume fraction can produce large changes in the drag force. This means that initial randomness of incoming particles produces variations in the drag coefficient, which in turn produce random force fluctuations. At high volume fractions, sufficiently downstream of the shock, the volume fraction corrected drag is much higher than either the pressure gradient or the inviscid unsteady force and accounts for the majority of the impulse imparted upon a particle.

3. *Inviscid unsteady force*

The inviscid unsteady force is given by

$$\boldsymbol{f}_{iu} = 4\pi R^3 \int_{-\infty}^{t} K_{iu}\left(\frac{a}{R}(t-\xi)\right)\left[\frac{\overline{D}}{Dt}\overline{\rho_g(\boldsymbol{u}_r-\boldsymbol{v}_r)}^S\right]_\xi \frac{a}{R} d\xi \,, \tag{15}$$

where $\boldsymbol{u}_r$ and $\boldsymbol{v}_r$ are the radial component of the fluid and particle velocities, respectively, in a coordinate system centered on the particle, and $\overline{D}/Dt = \partial/\partial t + \overline{\boldsymbol{u}}^V \cdot \nabla$ is the total derivative following the volume averaged fluid velocity. In the inviscid unsteady force, K_{iu} is the inviscid unsteady kernel with a functional form that is precisely known in the limit of small Mach numbers as (see Longhorn [26] and Parmar et al [33])

$$K_{iu}(\zeta) = e^{-\zeta}\cos(\zeta) \,. \tag{16}$$

where $\zeta = ta/R$ is a dimensionless time, which is non-dimensionalized by the acoustic time scale, where a is the speed of sound in the gas. Correspondingly, $\xi a/R$ is the non-dimensional time at which the density-weighted relative acceleration (the term in the square parenthesis) is evaluated. In the incompressible limit, the inviscid unsteady force is the added-mass force, which is proportional to the instantaneous relative acceleration between the particle and the surrounding gas. This direct relation between instantaneous acceleration and force is due to the infinite propagation speed of acoustic waves in the incompressible limit. In a compressible flow, due to the finite propagation speed of acoustic disturbances, the inviscid unsteady force is given by a convolution integral, where the kernel K_{iu} is the force response of a delta function relative acceleration. In (15), $\boldsymbol{u}_r$ as well as the undisturbed ambient gas density vary on the scale of the particle and thus $\rho_g(\boldsymbol{u}_r - \boldsymbol{v}_r)$ is averaged over the surface of the particle. Using properties of volume and surface integrals, the inviscid unsteady force expression can be rewritten as

$$\boldsymbol{f}_{iu} = \frac{4\pi}{3} R^3 K_{iu} \int_{-\infty}^{t} \left(\frac{a}{R}(t-\xi)\right) \left[\frac{\overline{D}}{Dt} \overline{(\rho_g(\boldsymbol{u}-\boldsymbol{v})}^{V} + \overline{\boldsymbol{r}\nabla\cdot(\rho_g(\boldsymbol{u}-\boldsymbol{v})}^{V}) \right]_{\xi} \frac{a}{R} d\xi \,, \tag{17}$$

where $\boldsymbol{r}$ is the radial vector from the center of the particle. This was the form obtained by Parmar et al [33] (also see [5]).

The inviscid kernel is independent of the Reynolds number. In general, it is a function of Mach number defined with the relative velocity (i.e., K_{iu} is dependent on $M = |\boldsymbol{u}-\boldsymbol{v}|/a$). In our case, the Mach number of the post-shock flow is small, and we ignore this Mach number dependence and assume K_{iu} to be that given in (16). However, this form has been derived for an isolated particle. In the present case of a distribution of particles, the presence of the neighboring particles will influence the inviscid unsteady force, which should be modeled as a volume fraction correction to K_{iu}. We currently have very little information on the volume fraction effect on the inviscid unsteady kernel, and as a result this dependence is ignored in the present point particle model.

4. *Viscous unsteady force*

In general, the force expression given in (9) includes the viscous unsteady contribution as well. This force is known as the Basset history force, and it arises from the time-dependent viscous diffusion of vorticity produced at the surface of the particle. It is written in terms of a convolution integral similar to (15), but with a viscous unsteady kernel K_{vu}. Unfortunately, the viscous unsteady kernel remains very difficult to model even for incompressible flows, since it depends not only on Reynolds and Mach numbers but on the time-dependent nature of relative acceleration. Fortunately, over the short time scale of shock-particle interactions, inviscid contributions $\boldsymbol{f}_{pg}$ and $\boldsymbol{f}_{iu}$ dominate, while over longer time scale quasi-steady force $\boldsymbol{f}_{qs}$ is the dominant contribution. Hence, for lack of precise understanding, we ignore the viscous unsteady force.

5. *Application to shock-particle interaction*

The undisturbed flow properties, such as $\boldsymbol{u}$, ρ_g and $D\boldsymbol{u}/Dt$ at the particle location are known in terms of the pre and post-shock states of the gas and the location of the particle with respect to the shock. The pre-shock gas density and pressure are given by their ambient values ρ_0 and p_0, while their post-shock values $\rho_1 = \rho_e$ and $p_1 = p_e$ are given by the multiphase shock equilibrium conditions, as detailed in section II B. (Subscripts 0 and 1 indicate upstream and downstream of the shock, respectively). The velocities must be adjusted to account for the change in the frame of reference. In the shock-attached frame the pre-shock gas velocity is the shock velocity in the lab frame (i.e., $\boldsymbol{u}_0 = u_s \boldsymbol{e}_x$), while the post-shock gas velocity is $\boldsymbol{u}_1 = (u_s - u_e)\boldsymbol{e}_x$, where u_e is the post-shock velocity in the lab frame. The undisturbed planar shock flow at the macroscale seen by the ith particle is fully defined and can be used along with the particle velocity and acceleration to explicitly compute the surface and volume averages over the particle in (10) and (11) as

$$\tilde{\boldsymbol{f}}_{qs,i} = \frac{3}{4}\frac{1}{\tilde{\rho}_p}\Big(\tilde{\rho}_1(\tilde{\boldsymbol{u}}_1 - \tilde{\boldsymbol{v}}_i)\tilde{\psi}_i + \tilde{\rho}_0(\tilde{\boldsymbol{u}}_0 - \tilde{\boldsymbol{v}}_i)(1-\tilde{\psi}_i)\Big)\Big|(\tilde{\boldsymbol{u}}_1 - \tilde{\boldsymbol{v}}_i)\tilde{\psi}_i + (\tilde{\boldsymbol{u}}_0 - \tilde{\boldsymbol{v}}_i)(1-\tilde{\psi}_i)\Big|\frac{24}{Re_i}\Phi \,, \tag{18}$$

$$\tilde{\boldsymbol{f}}_{pg,i} = \frac{6}{\tilde{\rho}_p}\tilde{\psi}_i(1-\tilde{\psi}_i)(\tilde{p_1} - \tilde{p_0})\boldsymbol{e}_x \,. \tag{19}$$

The above force expressions have been non-dimensionalized, with the particle diameter $d = 2R$ as the length scale, the sound speed of the pre-shock ambient fluid a_0 as the velocity scale, and $m_p a_0^2/d$ as the force scale. All gas properties, such as density and viscosity are scaled by their value in the pre-shock ambient state. In the above $\tilde{\psi}_i = \tilde{x}_i - \tilde{x}_s$ is the non-dimensional streamwise location of the ith particle with respect to the frozen shock location ($\tilde{x}_s$). For the inviscid unsteady force we obtain

$$\tilde{\boldsymbol{f}}_{iu,i} = \frac{12}{\tilde{\rho}_p} \int_0^\infty K_{iu}(\zeta) \Big[\big(\tilde{\rho}_1 \tilde{u}_1 - \tilde{\rho}_0 \tilde{u}_0 \big) \tilde{\psi}^2 \tilde{u}_s \Big]_{\tau - \zeta} d\zeta \;\; \boldsymbol{e}_x \, , \tag{20}$$

where we have changed the variable of integration to $\zeta = a(t - \xi)/R$. Though the integral goes from zero to infinity, the relative acceleration within the square parenthesis is non-zero only during the time interval during which the the shock crosses the particle. The convolution integral can be explicitly integrated using (16) for the kernel that assumes a frozen particle in the laboratory frame. The resulting expression is somewhat complicated and is given in Appendix A.

In preparation for simulating a bed of particles, the force model discussed above was validated for the case of shock propagation over an isolated particle. Figure 3 shows a comparison of the non-dimensional drag forced obtained from the point particle force model, with that obtained by experiments as well as a fully resolved direct numerical simulation (DNS), [31]. Both the DNS and experimental data are obtained from Sun et al. [43]. The drag coefficient is defined as $C_D = |\boldsymbol{f}_{gp}|/(\frac{1}{2}\rho_g \pi R^2 |\boldsymbol{u}_p|)$. For the DNS, a body-fitted finite volume method was used, and as such the particle remains frozen as it is swept by the shock. The results show an excellent agreement between the DNS and the point particle model as far as the initial rapid increase in the force, the peak value of the drag coefficient, and the time at which this peak is realized. During this early period, most of the impulse imparted to the particle is due to inviscid mechanisms. The model deviates slightly from the DNS and the experiments at intermediate times, but at long times the steady drag coefficient is captured by the quasi-steady portion of the drag model. The deviation between the DNS data and the point particle model at intermediate times is due to both the functional form of the inviscid unsteady kernel and the neglected unsteady viscous effects.

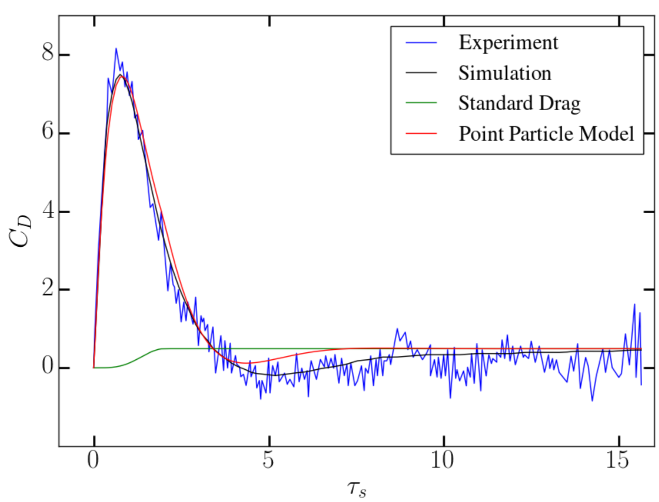

FIG. 3: The non-dimensional drag force for a shock passing over an isolated particle. The point particle force model discussed presently is compared to experimental and direct numerical simulation data for a frozen particle. The point particle model captures the net momentum impulse well.

E. Soft-sphere model of particle-particle interaction

The discrete element method tracks individual particles in the Lagrangian frame and allows detection of particle-particle interaction. A soft-sphere collision model allows for the particles to have a small overlap and uses a spring-dash-pot model to calculate normal and tangential forces. We consider perfectly smooth spheres where there is no tangential interaction. In the case of interaction between the ith and jth particle, the normal collisional force according to the soft-sphere model is

$$\boldsymbol{f}_{ij} = \left(k_n \delta_n \boldsymbol{n} - \gamma_n v_n \boldsymbol{n}\right). \tag{21}$$

Here δ_n is the normal overlap distance, $\boldsymbol{n}$ is the normal unit vector along the direction between the two particle centers, and v_n is the magnitude of the relative velocity. The spring coefficients for stiffness (k_n) and damping (γ_n) are derived using classical contact mechanics [1, 7, 12, 22, 40, 42, 51]. These coefficients are highly dependent upon the normal coefficient of restitution (e), a ratio of the post-collision velocity v_c' and the pre-collision velocity v_c, which in turn controls how much kinetic energy is lost due to an inelastic collision:

$$e = \frac{-v_c'}{v_c}. \tag{22}$$

The Hertzian force model within LIGGGHTS uses a nonlinear spring-dashpot for the normal forces using the following coefficients

$$k_n = \frac{4}{3}\Big(\frac{Y}{2(1-\nu^2)}\Big)\Big(\frac{R}{2}\delta_n\Big)^{1/2} \tag{23}$$

$$\gamma_n = -2\Big(\frac{5}{6}\Big)^{1/2}\frac{\ln e}{(\ln^2 e + \pi^2)^{1/2}}\Big(\frac{m_p Y}{2(1-\nu^2)}\Big)^{1/2}\Big(\frac{R}{2}\delta_n\Big)^{1/4} \geq 0\,. \tag{24}$$

This force model assumes that the two colliding spheres are of identical material properties and size. Mechanical properties of the particle including the Young's modulus Y, the Poisson ratio ν, as well as the normal coefficient of restitution are used to derive the spring coefficients consistent with the Hertzian collision time and the energy lost due to inelastic behavior of the colliding solids. Finally, the particle-particle interaction force of the ith particle, $\boldsymbol{F}_{pp,i}$ in (8), is obtained by summing the collisional force $\boldsymbol{f}_{ij}$ for all the jth particles in contact with the ith particle.

III. DATA PROCESSING

Figure 1 shows the distribution of particles from a typical simulation where the average pre-shock particle volume fraction of 10% increases to 56% in the equilibrium region downstream of the shock. The volume fraction remains low and uniform ahead of the shock (on the left) and the volume fraction steadily increases downstream of the shock (on the right). The problem is inhomogeneous along the streamwise direction, and is statistically homogeneous along the y and z-directions. The computational domain is binned in the streamwise direction in terms of planar slabs in order to compute averages. Each slab has a streamwise width of 5 particle diameters and is used to average the particle properties within the slab at a particular time, which will be called the *plane average*. The plane average is further averaged in time to obtain the *ensemble average*. Averaged quantities of interest include particle velocities, particle volume fraction and granular temperature. While the calculation of some of these quantities is straightforward, details of how the volume fraction and granular temperature are defined are given below.

A. Plane and ensemble averages

Results from different averaging processes are used to illustrate different statistical properties. Since the problem is statistically inhomogeneous only in the x-direction, we average over the transverse directions. We calculate the *plane average* of a quantity within thin slabs centered around an x-location. For particle properties this involves averaging over all the particles whose center lies within this thin slab at a particular time. For example, the plane-averaged streamwise velocity of the particle is defined by

$$\overline{v_x}(x, t_l) = \frac{1}{N_l} \sum_{i=1}^{N_l} v_{x,i}(t_l)\,, \tag{25}$$

where the overbar indicates a plane average and the sum is over all the N_l particles whose centers are within the slab at time t_l. The plane average is a function of x and time. Since the problem is statistically stationary, the plane average can be further augmented with an average over time to define the *ensemble average* as

$$\langle v_x \rangle(x) = \frac{1}{\big(\sum_{l=1}^{L} N_l\big)} \sum_{l=1}^{L} \sum_{i=1}^{N_l} v_{x,i,t_l}\,, \tag{26}$$

where the time average is over L time instances. We will show that the plane-averaged results at any given time are not the same as the ensemble-averaged results, due to spatial clustering of particles as they pass through the shock. These structures travel in the streamwise direction. Therefore their impact is observed only in the plane-averaged quantities, while their effect is averaged in the ensemble average.

B. Volume fraction definitions

Since Voronoi tessellation provides the cell volume associated with each individual particle, the local particle volume fraction associated with each particle can be calculated from (14). One way to calculate the average volume fraction within a slab (or at an x-location) is to simply average the local Voronoi volume fractions associated with all the particles within the slab. We can calculate the plane-averaged volume fraction $\overline{\phi}$ by counting the number of particles within a slab and then multiply by the ratio of the volume of a single particle to the volume of the slab. The ensemble-averaged volume fraction $\langle \phi \rangle$ can be calculated by further averaging over time to obtain

$$\overline{\phi} = \frac{V_p N_l}{V_{slab}} \quad \text{and} \quad \langle \phi \rangle = \frac{V_p}{V_{slab}} \frac{1}{L} \sum_{l=1}^{L} N_l = \langle N \rangle \frac{V_p}{V_{slab}}\,, \tag{27}$$

where N_l is the number of particle within the slab at the lth time instance and $\langle N \rangle$ is the mean number of particles within the slab averaged over L time instances. The above ensemble average definition is not the same as that obtained from averaging the Voronoi volumes, and in fact $\langle \phi \rangle$ can be related to Voronoi volumes by

$$\langle \phi \rangle = \big(\sum_{l=1}^{L} N_l\big) \left[\sum_{l=1}^{L} \sum_{i=1}^{N_l} \frac{1}{\phi_{v,i}} \right]^{-1}\,. \tag{28}$$

Here we will use the definition given in (27), since it correctly corresponds to the definition used in the multiphase shock relations presented in section II B.

We are also interested in observing variations in the Voronoi volume fraction downstream of the shock. Plane and ensemble averages for the Voronoi volume fraction, and variance of the Voronoi volume fraction are given by

$$\overline{\phi_v} = \frac{1}{N_l}\sum_{i=1}^{N_l}\phi_{v,i} \quad \text{and} \quad \langle\phi_v\rangle = \frac{1}{\left(\sum_{l=1}^{L} N_l\right)}\sum_{l=1}^{L}\sum_{i=1}^{N_l}\phi_{v,i}\,. \tag{29}$$

$$\langle\phi_v'^2\rangle = \frac{1}{\left(\sum_{l=1}^{L} N_l\right)}\sum_{l=1}^{L}\sum_{i=i}^{N_l}\Big[\phi_{v,i} - \langle\phi_v\rangle\Big]^2\,. \tag{30}$$

C. Granular temperature

Granular temperature is a measurement of random fluctuation energy manifested through the average velocity variance of the particles. The ensemble-averaged granular temperature is defined as

$$\langle T\rangle = \frac{\langle T_1\rangle + \langle T_2\rangle + \langle T_3\rangle}{3} \tag{31}$$

where the granular temperature contribution from each principle direction is defined as

$$\langle T_j\rangle = \frac{1}{3\left(\sum_{l=1}^{L} N_l\right)}\sum_{l=1}^{L}\sum_{i=i}^{N_l}\Big[v_{j,i} - \langle v_j\rangle^2\Big] \tag{32}$$

Due to the high slip velocity immediately after the shock, the bulk streamwise velocity changes rapidly within our computational slabs. Since the granular temperature is a measure of particle velocity variation from the bulk velocity, it is important that the change of bulk velocity within a slab be properly accounted for when calculating the granular temperature in the x-direction (i.e., in calculating $\langle T_1\rangle$). To account for this variation, we fit an interpolating polynomial to the ensemble-averaged x-velocity data and use this to define the perturbation velocity.

IV. RESULTS

A. Simulation cases

We chose three sets of particle and gas properties consistent with the multiphase shock relations given in section II B. Table III lists the values of volume fraction upstream and downstream of the shock, as well as the velocity, density, and pressure ratios across the shock for the three cases. Case 1 has an initial volume fraction of 10% which quickly compacts to a dense volume fraction of 56.6%. Case 2 is a more dilute configuration, with an initial volume fraction of 5%, which compacts to 26%. Due to the coupled nature of the multiphase shock relations, changing the initial volume fraction changes the gas density and pressure ratios across the shock. For Case 2, both the density and pressure ratios across the shock are about half those obtained for Case 1. The density ratio change is particularly important as it changes the post-shock particle to gas density ratio, which determines the particle phase relaxation length (a higher density ratio will lead to a shorter relaxation length). Additionally, a change in the particle volume fraction also affects the particle relaxation length, due to the volume fraction dependence of the quasi-steady drag (A lower volume fraction will correspond to a longer relaxation length). Due to these two effects, the relaxation length of Case 2 is expected to be significantly longer than that of Case 1. Case 3 has an initial volume fraction is 10% as did Case 1, however the ratio of specific heats of the particles and gas is set to zero. Physically this means there is no heat transfer between the gas and particle phases, the effect of which is a lower equilibrium volume fraction of 31% as well as a lower density ratio across the shock compared to those for Case 1. Together, these three cases contain a wide range of particle volume fractions along with a range of density ratios across the shock.

For each case, we performed a parametric study by running simulations with different values of normal coefficient of restitution e. The coefficient of restitution is a measure of how much kinetic energy a particle pair loses when undergoing collision. A coefficient of restitution of $e = 1$ corresponds to a perfectly elastic collision where no kinetic energy is lost. A coefficient of restitution of $e = 0$ corresponds to a perfectly inelastic collision where particles move at the same velocity post collision. For our parametric variation, we consider a range of between 0.4 and 1.0.

TABLE III: Multiphase shock properties

	Case 1	Case 2	Case 3
Pre-shock particle volume fraction : ϕ_0	0.1	0.05	0.1
Ratio of specific heats: δ	1	1	0
Equilibrium particle volume fraction: ϕ_e	0.5658	0.2564	0.3063
Gas velocity ratio: $\frac{u_e}{u_0}$	0.1771	0.1950	0.3264
Gas density ratio: $\frac{\rho_e}{\rho_0}$	11.68	6.551	3.974
Gas pressure ratio: $\frac{p_e}{p_0}$	13.56	7.705	11.28

One of our key findings is that after the passage of a shock, a random distribution of particles with spacing of uniform probability will not only see and increase in mean volume fraction, but will exhibit clustering at both the macro and microscales. We described and analyzed this in detail, in the remainder of this section, which is laid out as follows. Section IV B discusses the nature of particulate structures observed downstream of the shock. Section IV C quantifies these particulate structures with ensemble-averaged Voronoi statistics calculated upstream and downstream of the shock and compares these statistics to those for a perfectly random distribution of particles at comparable volume fractions. Section IV D discusses ensemble-averaged results for the granular temperature, the streamwise particle velocity, and the variance of the Voronoi volume fraction.

B. Post-shock Particulate Structure

In the shock-attached reference frame, we expect the system to be statistically stationary and the ensemble-averaged velocity and volume fraction to change monotonically from the pre-shock state to a post-shock equilibrium state. However, such an ensemble-averaged picture masks a traveling wave structure that persists downstream of the shock, which we observe in the DEM simulations. We identify wave-like structure by generating pseudocolor plots of the Voronoi volume fraction. To further illustrate this point, we will compare planar averages of particle volume fraction as well as streamwise velocity, computed at one time instant, to the corresponding ensemble-averaged statistics.

The observed post-shock structures in Figures 4, 5, and 6 are for Cases 1, 2, and 3, respectively. These figures show pseudocolor plots of Voronoi volume fraction projected onto the $x - z$ plane. For each case studied, the results are shown for three coefficients of restitution: the elastic limit where $e = 1$, an intermediate value where $e = 0.7$, and a strongly inelastic case where $e = 0.4$. A macroscopic wavy particulate structure is observed in all cases except for Case 1 in the elastic limit where $e = 1$. An analysis of the Voronoi volume statistics presented in later sections will show that there is indeed a structure present in this case, however, it is not easily observed in Figure 4. This wavy distribution of particle volume fraction is due to the volume-fraction-dependence of the quasi-steady drag. In other words, the instability arises from the gas-mediated particle-particle interaction. This macroscopic structure is particularly pronounced Cases 2 and 3 (Figures 5 and 6). As inelasticity is introduced by decreasing the coefficient of restitution, the amplitude of these waves increase indicating an increase in the cluster intensity. This indicates that the macroscopic structure induced by the gas-mediated particle-particle interaction is amplified by the dissipative nature of the collisional process. As a result, the intensity of particle clustering intensifies with particle inelasticity.

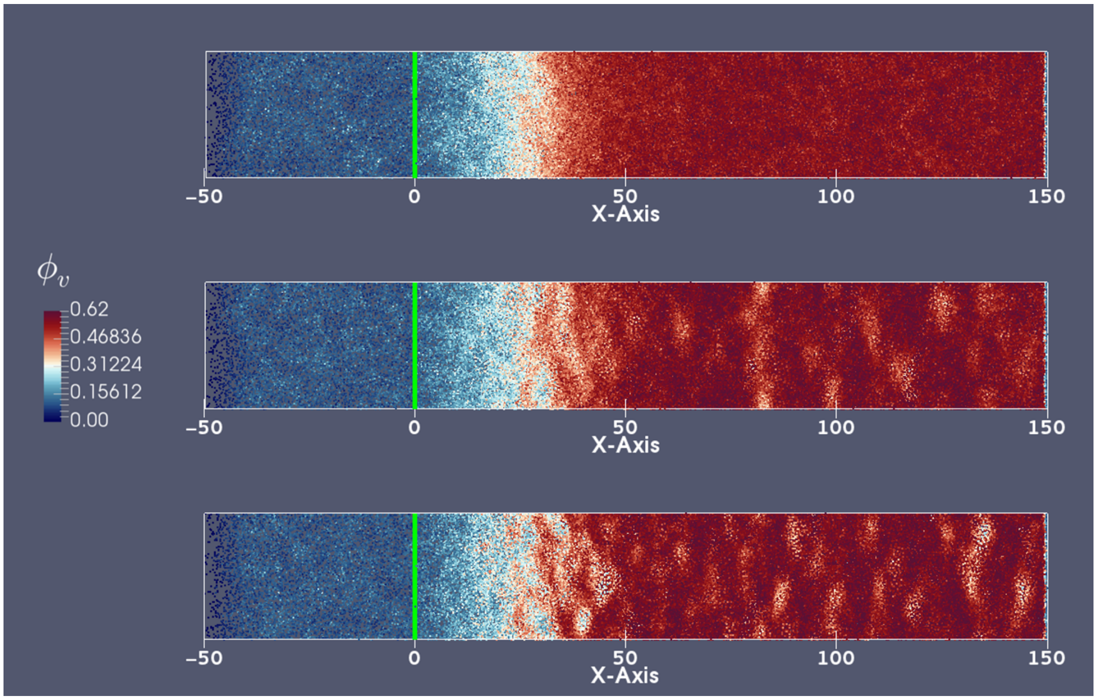

FIG. 4: A pseudocolor plot of the Voronoi volume fraction for Case 1. A green line at $x = 0$ shows the location of the planar shock. Three coefficients of restitution are plotted: $e = 1$ (top), $e = 0.7$ (middle), and $e = 0.4$ (bottom).

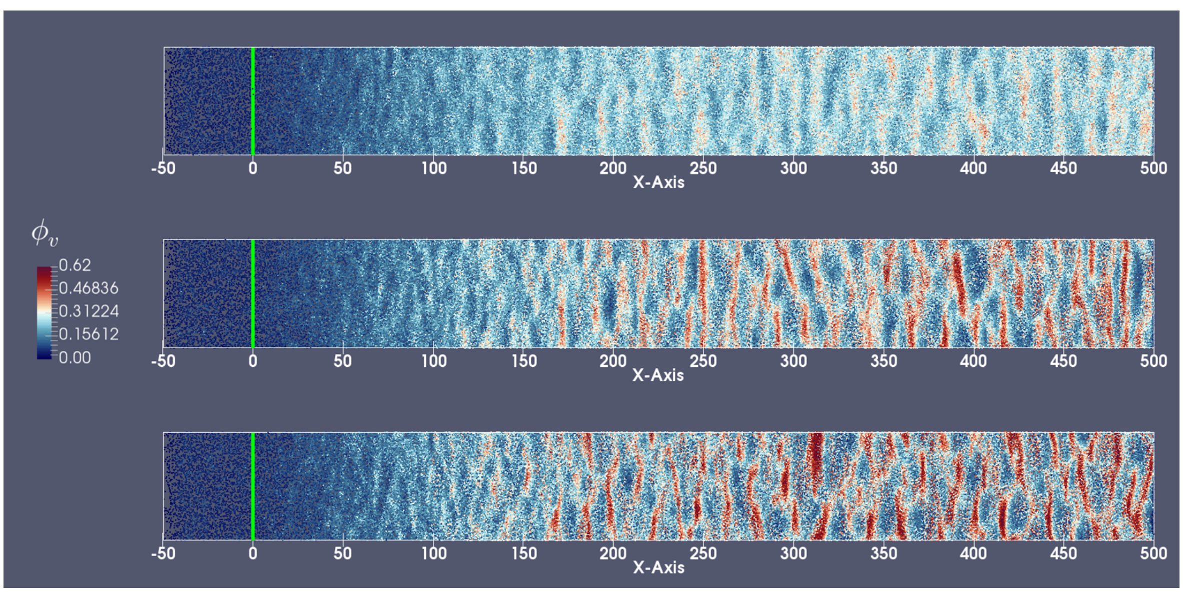

FIG. 5: A pseudocolor plot of the Voronoi volume fraction for Case 2. A green line at $x = 0$ shows the location of the planar shock. Three coefficients of restitution are plotted: $e = 1$ (top), $e = 0.7$ (middle), and $e = 0.4$ (bottom).

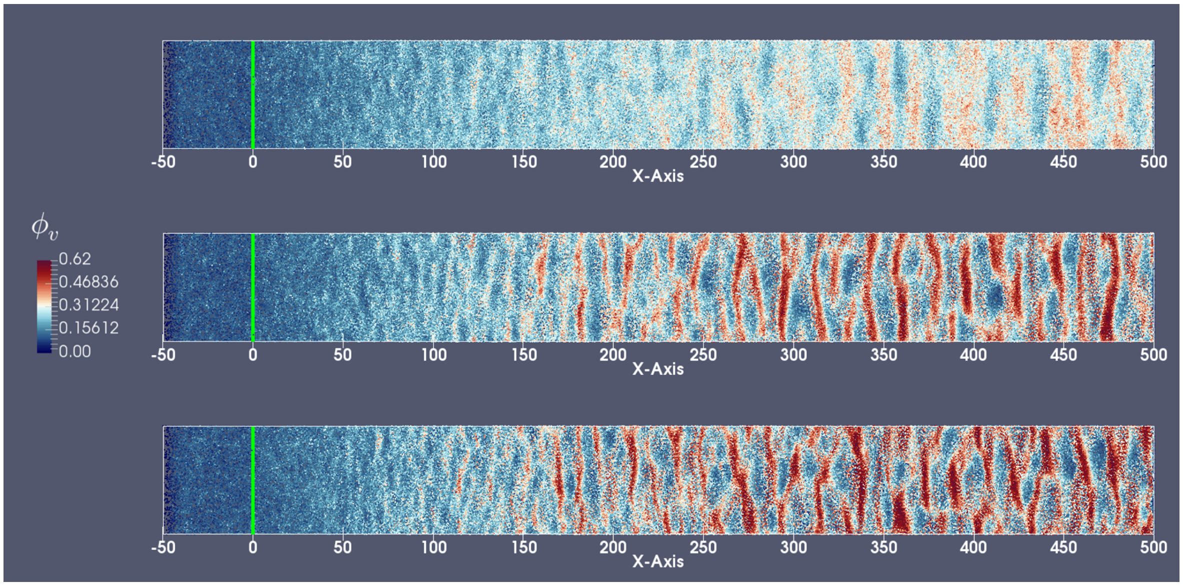

FIG. 6: A pseudocolor plot of the Voronoi volume fraction for Case 3. A green line at $x = 0$ shows the location of the planar shock. Three coefficients of restitution are plotted: $e = 1$ (top), $e = 0.7$ (middle), and $e = 0.4$ (bottom).

Fluidized-bed research has shown that volume fraction-dependent drag force produces macroscopic variations in volume fraction in the form of waves [13, 30]. Similarly, it is well understood that an initially excited particulate system (i.e., particles having random initial velocity), when allowed to cool due to inelastic collisions, results in clustering of particles at the microscale [19, 27]. This is due to the fact that after each collision, the paired particles lose momentum, reducing post collision separation. Thus, repeated collisions results in localized clusters of particles. In the present inelastic simulations, both these macro and microscale clustering mechanisms appear to be active.

Due to the conservation of mass, the ensemble-averaged volume fraction $\langle\phi\rangle$ downstream of the shock must approach the equilibrium volume fraction ϕ_e as the particles relax to the post-shock equilibrium velocity u_e. As can be seen in the wave pattern observed in Figures 4, 5, and 6, however, the plane-averaged volume fraction at a fixed-time, $\overline{\phi}$, even far downstream of the shock will clearly fluctuate about this equilibrium volume fraction. Plots of plane and ensemble-averaged volume fraction ($\overline{\phi}$ and $\langle\phi\rangle$), along with the plane and ensemble-averaged x-velocity of the particles ($\overline{v_x}$ and $\langle v_x\rangle$), are presented in Figures 7, 8, and 9. The ensemble-averaged volume fraction for all values of e approach the same post-shock equilibrium value. However, the rate of approach appears to be slightly influenced by inelastic collisions.

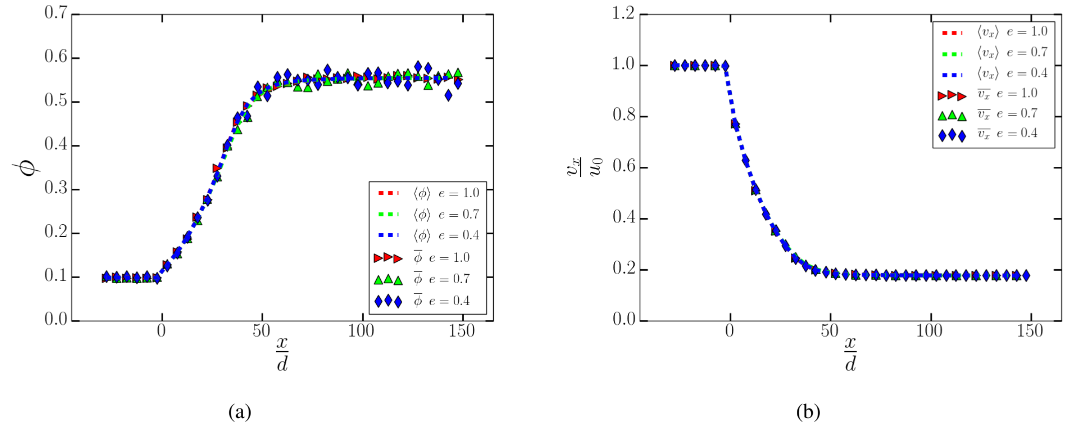

FIG. 7: Ensemble-averaged ϕ (a.) and x-velocity (b) compared with the fixed-time, planar averages for Case 1. The variation of $\overline{\phi}$ is small compared to the variation seen in cases with lower ϕ_e.

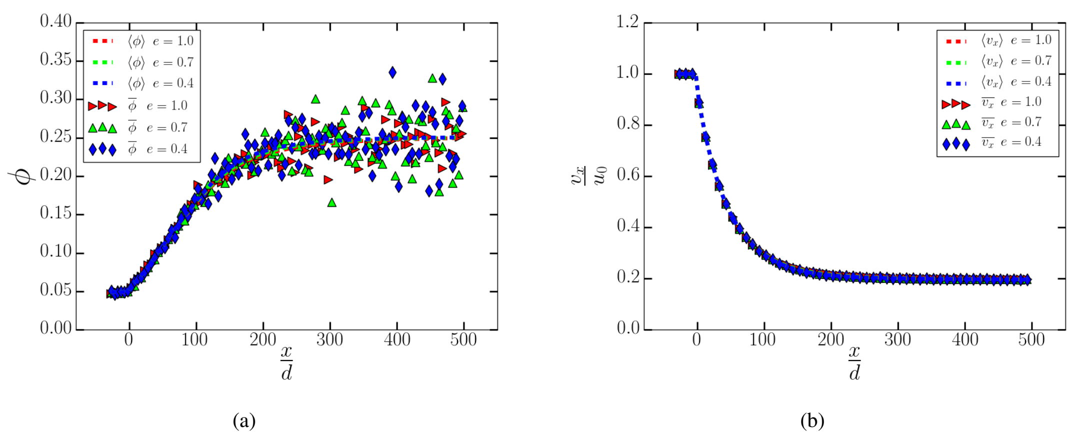

FIG. 8: Ensemble-averaged ϕ (a.) and x-velocity (b) compared with the fixed-time, planar averages for Case 2. Variations in $\overline{\phi}$ of almost 10% are seen both above and below the ensemble-averaged values.

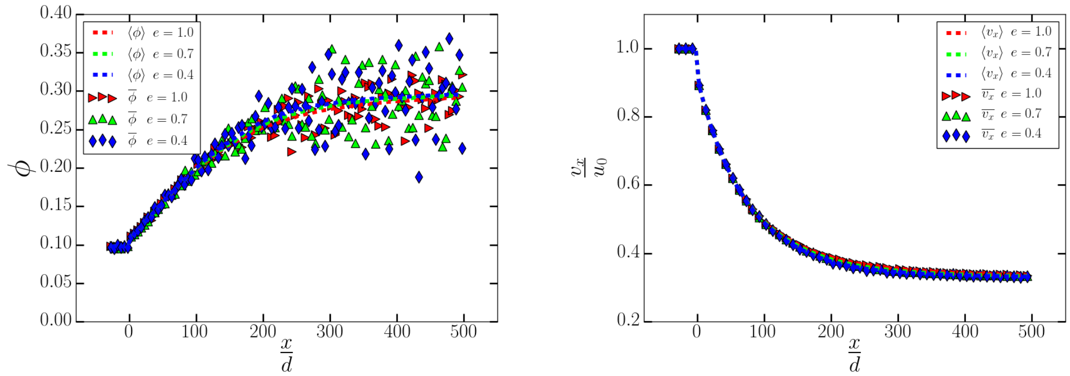

(a)

(b)

FIG. 9: Ensemble-averaged ϕ (a.) and x-velocity (b) compared with the fixed-time, planar averages for Case 3. Similar to Case 2, Variations in $\overline{\phi}$ of almost 10% are seen both above and below the ensemble-averaged values.

As expected by the presence of a wave-like structure, the plane-averaged volume fraction plotted at a specific time varies along the x-direction and deviates from the ensemble average. For Case 1, the equilibrium volume fraction of $\phi_e = 0.57$ is within a few percent of the close-packing limit of $\phi = 0.64$. This puts a physical upper limit on the possible local volume fractions. Due to this constraint, the variation in $\overline{\phi}$ is small in Figure 7 compared to the variation at lower volume fractions observed in Figures 8 and 9. In all three cases, the plane average of the elastic collision sub-cases has the least deviation from the ensemble average. As inelasticity is increased, the deviation from the ensemble average increases.

Unlike the particle volume fraction, the particle x-velocity does not vary greatly between the ensemble average $\langle v_x \rangle$ and the plane average $\overline{v_x}$. The particle x-velocity fluctuations are small compared to the bulk flow speed, and the effect of the wave structure upon the bulk x-velocity is negligible. This indicates that the dense particulate structures observed in Figures 4, 5, and 6 are frozen in the post-shock equilibrium state. Since all particles, clustered or otherwise, travel at the post-shock gas velocity in the equilibrium state, there is no drag, and the volume-fraction dependence of drag becomes irrelevant.

It should be noted, that even though the volume fraction in Case 1 does pass through volume fraction values seen in Cases 2 and 3, there is far less deviation from the ensemble average at these volume fractions. Another factor contributing to the difference is the time scale of response for the particles, characterized by the particle time scale

$$\tau_p = \frac{\frac{\rho_p}{\rho_g} d^2}{18 \nu_g \Phi} \,. \tag{33}$$

The particle relaxation time scale is much smaller in Case 1 due to the smaller post-shock density ratio $(\rho_p/\rho_g) = (\rho_p/\rho_0)(\rho_0/\rho_e) = 8.56$ compared to the post-shock density ratios $(\rho_p/\rho_g) = 15.26$ and 25.1 in Cases 2 and 3. Also contributing to the larger particle relaxation time scale are the Reynolds number and volume fraction correction Φ detailed in (12). A lower particle time scale in Case 1 means the system relaxes to the equilibrium state more quickly, approximately 50 particle diameters compared to 200 diameters in Case 2 and 400 diameters in Case 3.

Our model simulations show a remarkable traveling wave structure that forms downstream of the shock. This observed structure has two primary causes. A macroscopic structure is induced by the gas-particle interaction via the volume fraction dependent quasi-steady drag force, and a clustering mechanism at the microscale induced by inelastic collisions. This traveling wave structure cannot be captured by ensemble averages of either the volume fraction ϕ, or the x-velocity. Planar averages, however, show that there is a high degree of volume fraction variance caused by the clustering behavior. There is little variance in the x-velocity since velocity fluctuations are small compared to the bulk velocity. This variance in the volume fraction is discussed further below.

C. Voronoi Volume Statistics

In the previous section, we showed that there is a traveling wave particulate structure caused by macroscopic and microscopic mechanisms. In this section, we investigate ensemble-averaged Voronoi volume statistics upstream and downstream of the shock. We compare the simulation statistics against corresponding statistics of a random distribution of particles of uniform probability. While the ensemble-averaged mean Voronoi volume is independent of the coefficient of restitution, the distribution of Voronoi volume about this mean changes significantly as the coefficient of restitution is varied. This demonstrates the role of inelastic collisions in the particle clustering behavior.

Particles enter the simulation domain with a random spatial distribution of uniform probability. Due to the randomness of particle location, there is natural variation in the Voronoi volume associated with this upstream uniform particle distribution. As the particles pass through the shock, this variation in Voronoi volume naturally changes due to the compaction of the system to a higher mean volume fraction. Additionally, clustering at the macroscale due to volume fraction dependent drag, as well as microscale clustering due to inelastic collisions, cause further variations in the Voronoi volume distribution. We quantify the degree of excess clustering due to these additional effects using histograms of the Voronoi volume. But first, it is important to understand the distribution of Voronoi volume statistics of a randomly distributed particles of uniform probability for comparison.

A number of researchers have studied the distribution of Voronoi volumes in 2-D and 3-D for random distributions of point particles, 2-D hard disks, and 3-D hard-spheres [16, 23, 41, 44]. The work of Kumar & Kumaran [41] is of particular relevance as they studied the statistics of Voronoi volume for a random Poisson process [44] with the added positional constraint that the minimum distance between any two particle pair be larger than the sum of their radii. They defined free Voronoi volume, V_f, as the volume in excess of the minimum possible Voronoi volume at close ordered packing, corresponding to both the face centered cubic (FCC) and the hexagonal close-packed latices. The mean free Voronoi volume can be expressed by

$$\langle V_f \rangle = \langle \frac{V_p}{\phi_v} \rangle - \frac{3\sqrt{2}V_p}{\pi} \ , \tag{34}$$

where the first term corresponds to the mean Voronoi volume, while the second term is the smallest possible Voronoi volume corresponding to FCC packing. They observed the following 3Γ function to fit the Voronoi volume distribution quite well

$$f(V_f) = \frac{\delta \alpha^{m/\delta^2}}{\Gamma(m/\delta^2)} V_f^{(m/\delta - 1)} e^{(-\alpha V_f^{\delta})}. \tag{35}$$

There are three parameters that define the 3Γ function. The parameters δ and m are presented as functions of the mean volume fraction $\langle \phi \rangle$, and the final parameter, α, is constrained to be a function of the other two parameters, δ, and m, so that the mean of the above distribution becomes equal to the mean free Voronoi volume, $\langle V_f \rangle$. This gives the relation

$$\alpha = \left[\frac{\Gamma((m+\delta)/\delta^2)}{\Gamma(m/\delta^2)\langle V_f \rangle} \right]^{\delta} \ . \tag{36}$$

Higher order moments of Equation (35) can be explicitly calculated, and can then be used to obtain central moments such as the variance, skewness, and kurtosis. The n-th moment can be expressed as

$$\langle V_f^n \rangle = \frac{\Gamma((m+n\delta)/\delta^2)}{\Gamma(m/\delta^2)\alpha^{n/\delta}} \ . \tag{37}$$

We expect the pre-shock distribution of particles to be well approximated by the above 3Γ function. For all three cases, the Voronoi volumes of all the particles upstream of the shock are put into a histogram and compared to the theoretical 3Γ function in Figures 10, 11, and 12. In these figures, the upper left-hand plot shows the particle distribution upstream of the shock, while the remaining three plots show the distribution far downstream of the shock for three different values of e. Note that in each case, the data provided by Kumar & Kumaran [41] was used to obtain the parameters γ, m, and α for a known local volume fraction. For Cases 1 and 3, where the initial volume fraction is $\phi_0 = 0.1$, the theoretical 3Γ function matches the upstream DEM Voronoi volumes. For Case 2, where $\phi_0 = 0.05$, the upstream DEM Voronoi data has a slightly smaller mean, and is slightly skewed towards smaller volumes. This discrepancy could be due to the insertion algorithm used at the inflow boundary at the lower volume fraction.

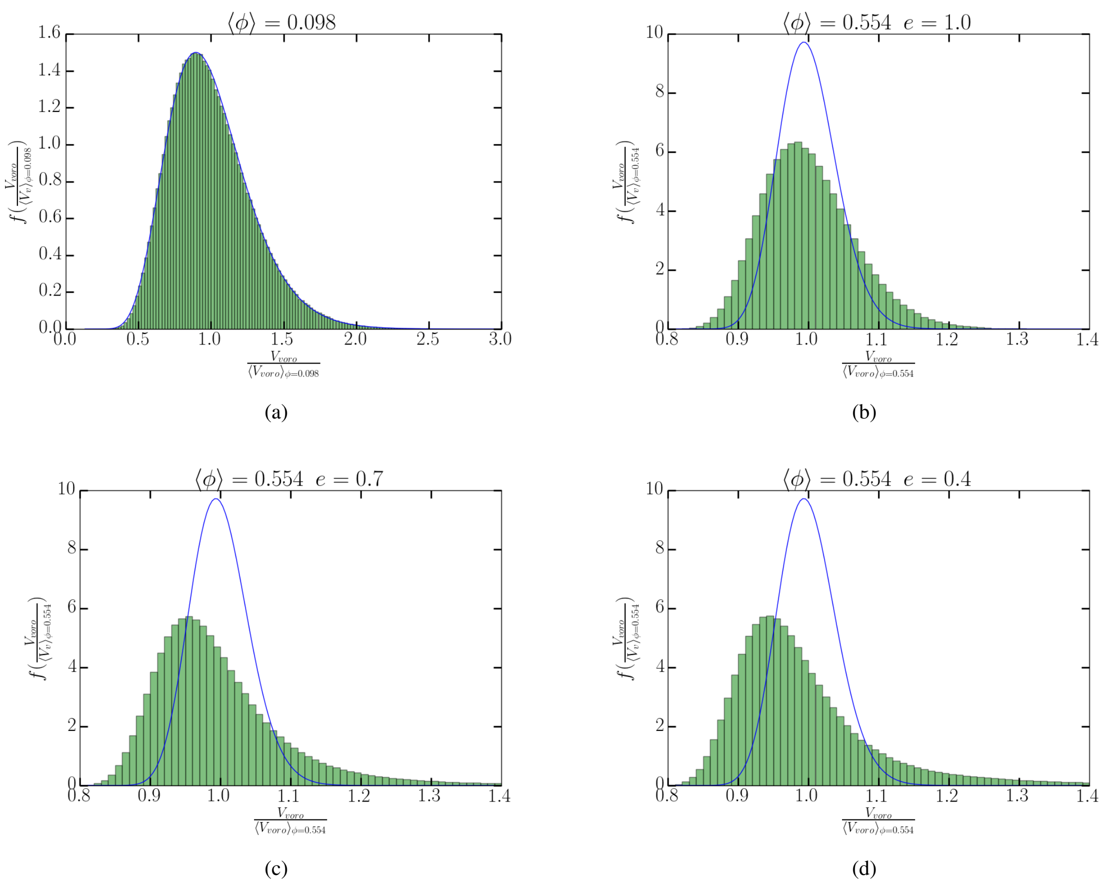

FIG. 10: Histogram Voronoi volume data (green) resulting from Case 1 is plotted against the 3Γ distribution (blue). Values are shown upstream of the shock at the initial volume fraction $\phi_0 = 0.1$ and downstream of the shock for various coefficients of restitution at the equilibrium volume fraction $\phi_e = 0.554$. Upstream of the shock the histogram-ed DEM data and the 3Γ distribution are in excellent agreement. However, downstream of the shock there is a departure from the 3Γ distribution for all coefficients of restitution including the elastic limit ($e = 1$). As inelasticity is increased, the DEM data shifts towards smaller Voronoi volumes.

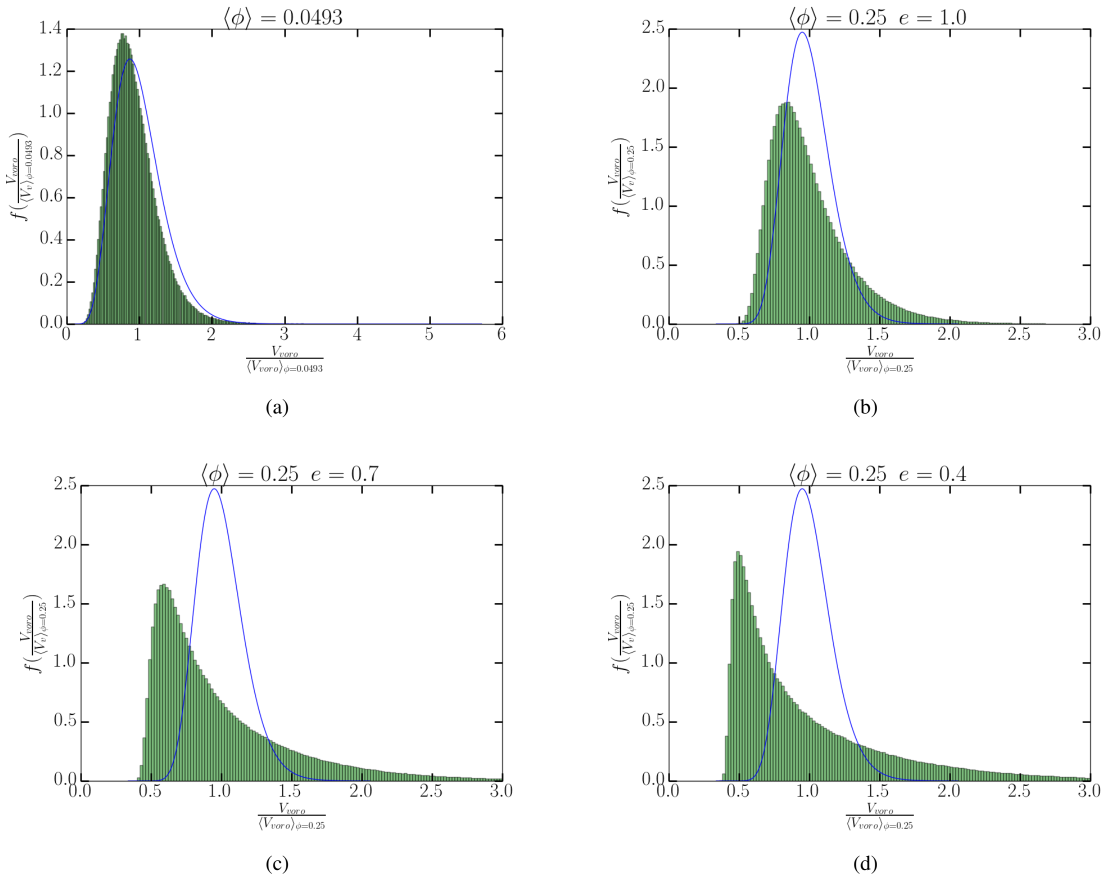

FIG. 11: Histogram Voronoi volume data (green) resulting from Case 2 is plotted against the 3Γ distribution (blue). Values are shown upstream of the shock at the initial volume fraction $\phi_0 = 0.05$ and downstream of the shock for various coefficients of restitution at the equilibrium volume fraction $\phi_e = 0.25$. As inelasticity is increased, there is a much more pronounced shift than was observed in Figure 10.

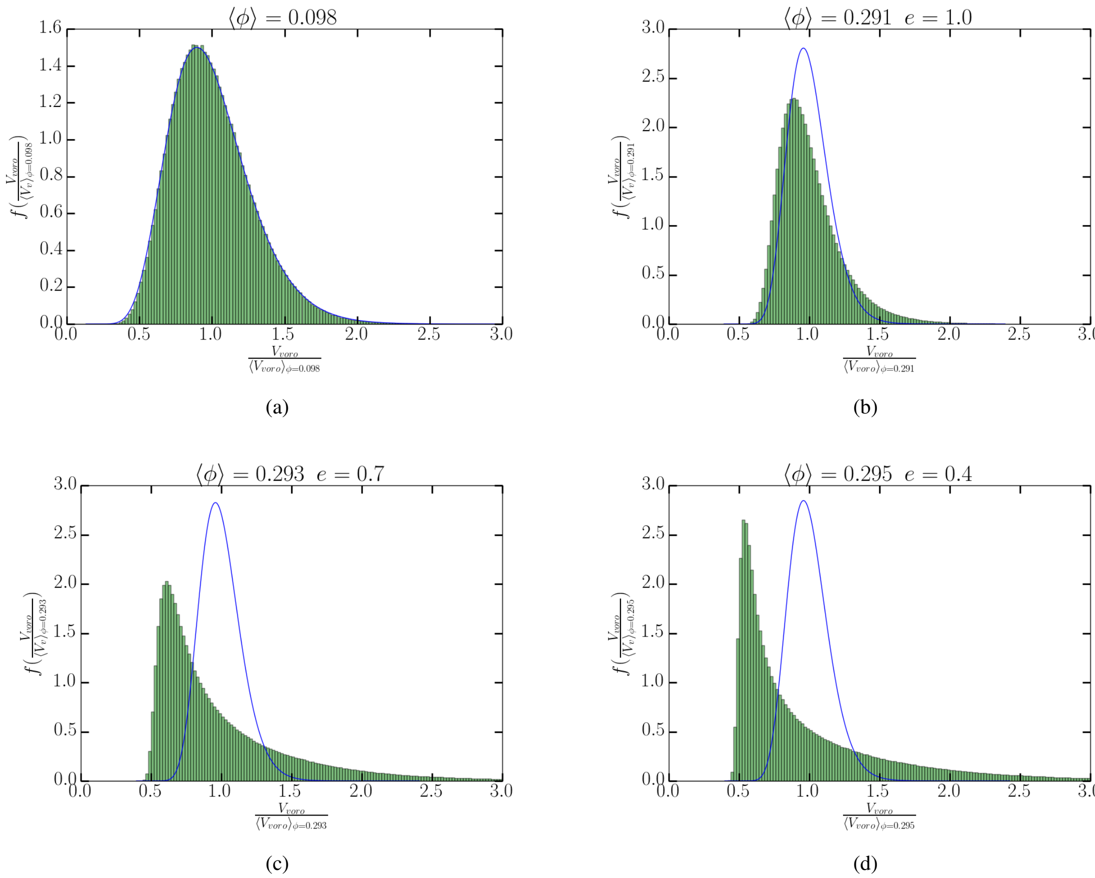

FIG. 12: Histogram Voronoi volume data (green) resulting from Case 3 is plotted against the 3Γ distribution (blue). Values are shown upstream of the shock at the initial volume fraction $\phi_0 = 0.1$ and downstream of the shock for various coefficients of restitution at the equilibrium volume fraction $\phi_e = 0.295$.

Far downstream of the shock, the ensemble-averaged volume fraction approaches the equilibrium volume fraction. However, the Voronoi volume distribution is expected to deviate from the ideal 3Γ function due to the wave structure observed in the particle concentration. In Figures 10, 11, and 12, we additionally present the normalized histograms of the Voronoi volume evaluated far downstream of the shock. We compare the histograms from the DEM data to the theoretical 3Γ function at the corresponding equilibrium volume fraction. In the elastic limit ($e = 1$), downstream of the shock, the peak of the DEM distributions are slightly skewed to the left compared to the 3Γ function. This is more pronounced in Figures 11 and 12 for Cases 2 and 3. This shift is due to the macroscale clustering of particles induced by the volume fraction dependent drag force. As collisions are made inelastic by lowering the coefficient of restitution, the DEM distributions shift further, with the peak moving towards small Voronoi volumes. This shift is compensated by a long tail for higher Voronoi volumes. Again, this shift due to inelastic collisions is most evident in Cases 2 and 3, where sharp distributions develop for the inelastic coefficients ($e < 1$). Case 1 is constrained by the close-pack limit and therefore retains a smoother distribution.

The theoretical 3Γ function does not capture the DEM distribution downstream of the shock due to the traveling wave-like particle concentration variation. In an attempt to illustrate the effect of such a traveling wave-like particle clustering, a sinusoidally varying plane-averaged volume fraction is considered. A traveling wave of amplitude A is added to the ensemble average as

$$\overline{\phi}_{wave} = \langle \phi \rangle + A \sin\left(\frac{2\pi}{\lambda}(x - ct)\right) , \tag{38}$$

where λ is the wavelength and c is the phase speed of the traveling wave. With this model, for a given A and λ, the sinusoidally perturbed local volume fraction at each x-location is constructed. At each x location, and correspondingly each local value of $\overline{\phi}_{wave}$, the 3Γ function is computed. An average 3Γ function can then be computed which accounts for the range of volume fractions within the wavy structure. Figure 13 presents the averaged 3Γ distribution sampled over a single wavelength. All three cases are shown, and for each case, a number of amplitudes values (A) are presented. For case 1, the peaks of the volume fraction wave must remain under the close-pack limit, and as a result only a limited range of A is tested. In all cases, increasing A shifts the distribution towards the left, and broadens it. This is consistent with the trends observed in Figures 10, 11, and 12. For large amplitudes, in Figures 13b and 13c we observe the volume fraction distribution to sharpen in a manner similar to the inelastic cases downstream of the shock. It is also clear that no value of A precisely match with the distributions seen in Figures 10, 11, and 12, which indicates the fact that the structures observed in the DEM are not perfectly sinusoidal, but are three-dimensional.

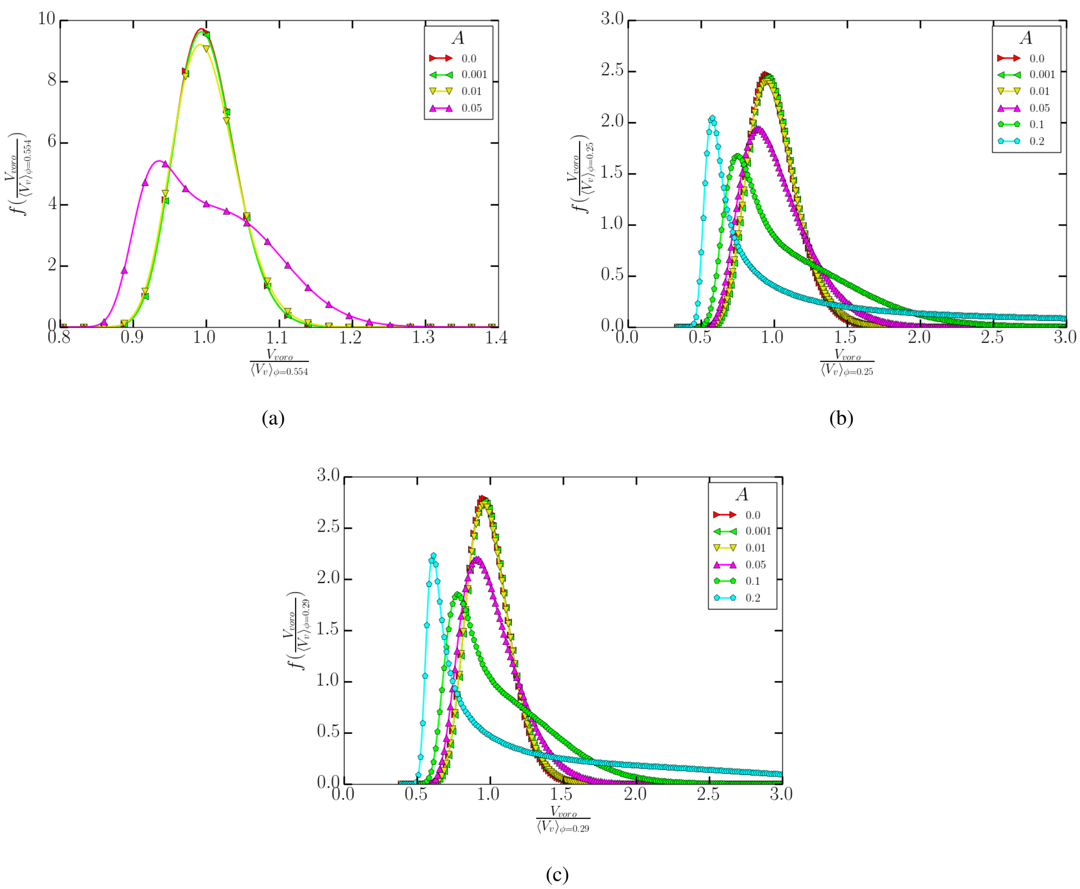

FIG. 13: Sinusoidally varying plane-average of to the 3Γ distribution for three volume fractions corresponding to the equilibrium volume fractions ϕ_e downstream of the shock for Cases 1 (a), 2 (b) and 3 (c). A number of values for the amplitude are shown. As the amplitude of the wave increases the distribution shifts toward lower volumes similar to the downstream particles observed in Figures 10, 11 and 12.

The theoretical 3Γ distribution has proven to be a useful tool by establishing a baseline for random distribution of particles against which the DEM Voronoi statistics downstream of the shock are compared. Deviation from the 3Γ distribution is a clear indicator of the particle structure that was observed in the previous section. The 3Γ distribution is used in the next section when discussing the ensemble-averaged variance of Voronoi volume fraction.

D. Ensemble-Averaged Results

In this section, we discuss the results for the three different cases in sequence. We focus on ensemble-averaged statistics for the particle velocity and volume fraction, as well as granular temperature and Voronoi volume fraction variance profiles for each of the cases. The ensemble averaged quantities do not capture the traveling wave structure of the post-shock particle distribution. The traveling wave-like structure is only observed when taking higher order moments of the data.

1. Case 1

The ensemble-averaged streamwise component of particle velocity and particle volume fraction for Case 1 are shown in Figure 7. The product of the two is the net streamwise flux of particles, which must be a constant. Thus, as the streamwise velocity decreases from the pre-shock to post-shock values, in the shock-attached frame, the particle volume fraction correspondingly increases to the final equilibrium volume fraction. The results for the different coefficient of restitutions nearly collapse, indicating the independence of these ensemble-averaged quantities from the details of the collision process. As can be expected, the streamwise evolution of mean particle velocity, and accordingly, the streamwise variation of mean particle volume fraction, is most influenced by particle response time, which in turn depends on the particle-to-gas density ratio (see (33)).

An upper bound for the particle time scale is achieved when $\Phi = 1$, corresponding to zero Reynolds number limit for an isolated particle (i.e., for $Re = 0$ and $\phi = 0$). Using the particle-to-gas density ratio in the post-shock flow ($\rho_p/\rho_e = 8.56$), and a gas kinematic viscosity of 13.5 mPa s, we obtain an upper bound for the particle time scale as $\tau_{upper} = 6.4 \times 10^{-4}$ s. From this value and the post-shock gas velocity of 6075 cm/s, an upper bound relaxation length scale of approximately 600 particle diameters is calculated. However, this is an overestimate, since particle Reynolds number is much larger than unity, and as a result $\Phi \gg 1$. Simulation results show that the particle relaxation length scale is actually about 50 particle diameters, an order of magnitude smaller than the calculated upper bound. This discrepancy illustrates how the nonlinear volume fraction dependent drag acts to rapidly equilibrate the particles.

While the mean particle velocity and volume fraction are independent of coefficient of restitution, we expect quantities that depend on the inter-particle collision process to vary with e. Of particular interest is how the granular temperature changes when varying e. Recall that particles initially enter the computational box in a cooled state with zero velocity fluctuation. After encountering the shock, the aerodynamic forces increase as do the force fluctuations. These force fluctuations cause the particles to accelerate at different speeds and collide, generating random fluctuation energy. At this point there are two modes by which this new found fluctuation energy dissipates. The first mode is the gas induced drag force. Immediately downstream of the shock, the gas induced drag force works to increase both the mean and fluctuating particle velocity. Once the particles have approached the post-shock equilibrium velocity, the effect of gas induced drag force is to damp the velocity fluctuation. A particle velocity that differs from that of the surrounding gas velocity causes a drag force that drives the particle velocity toward that of the gas. The second mode of energy dissipation is energy lost due to inelastic collisions. Energy fluctuations introduced due to the shock are eventually dissipated, and the particles return to a perfectly cooled state.

Figure 14, shows the ensemble-averaged granular temperature variation plotted as a function of x. The temperature is scaled by the peak value of granular temperature, while x is scaled by the x-location of the peak value. Figure 15 shows the peak values for varying coefficients of restitution. This figure is non-dimensionalized by the incoming pre-shock velocity of the gas and the particle diameter. The peak value of the granular temperature decreases as the degree of inelastic collisions is increased (coefficient of restitution e is decreased) since inelastic collisions provide a mechanism for the fluctuating kinetic energy to dissipate. Under the aforementioned scaling, the temperature data seems to somewhat collapse into a self-similar curve. The collapse is better for the lower coefficients of restitution. In the elastic limit ($e = 1$), the width of the temperature plot appears slightly wider than for the inelastic coefficients ($e < 1$). Immediately after the shock, at $x = 0$, the plots do not collapse, and achieve a magnitude close to the peak value in the elastic limit ($e = 1$). The lack of collapse close to the shock is due to the nature of the pressure gradient and inviscid unsteady forces. These near-impulsive forces impart rapid acceleration to the particles, but these forces quickly decay due to their short range of influence.

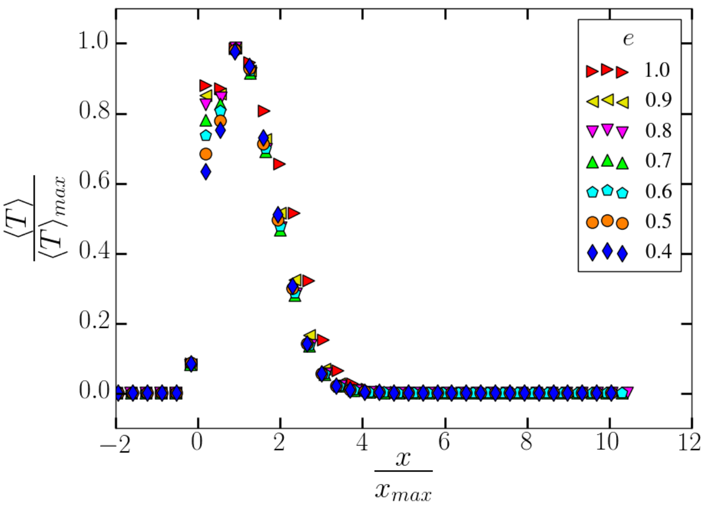

FIG. 14: Case 1: Variation in granular temperature scaled by the peak granular temperature as well as the x-location of the peak. The elastic limit ($e = 1$) is shown to break the self-similar collapse.

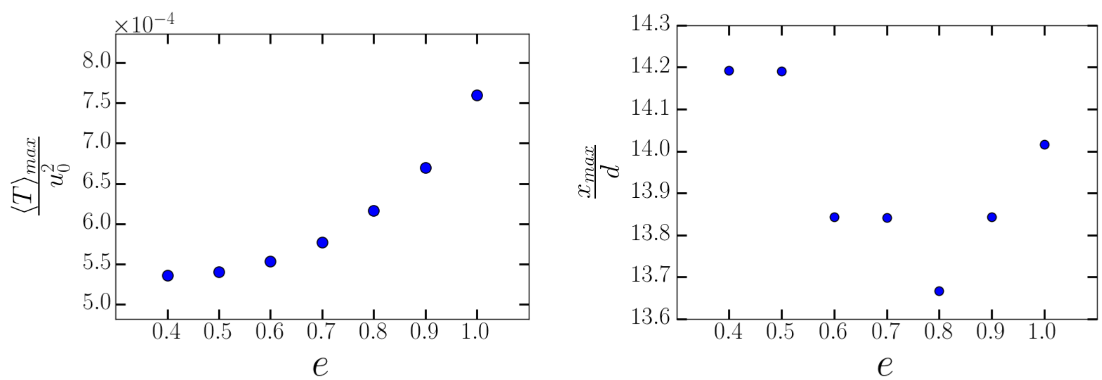

(a)

(b)

FIG. 15: Case 1: The peak non-dimensional granular granular temperature (a) is shown to increase while the x-location of the peak (b) moves towards the shock as the coefficient of restitution approaches 1.

The quasi-steady drag force is the long acting force which drives the long term evolution of the system. Figure 3 shows that the force exerted on the particles is initially dominated by the inviscid contributions, whose magnitude is large, but short lived. Simple analysis shows that the change in particle velocity across the shock at the end of this inviscid phases scales as $(\rho_e/\rho_p)(u_0 - u_e)$ [24, 25]. In the shock-attached frame, this results in a particle velocity of $v_p = u_0 - \left(\frac{\rho_e}{\rho_p}\right)(u_0 - u_e)$, immediately downstream of the shock due to the rapid action of the inviscid pressure gradient and added-mass forces. From the multiphase shock properties given in Table III, we can estimate the particle velocity to rapidly change from the pre-shock value of u_0 to a value of about $0.9\, u_0$. This rapid variation in the particle velocity, when averaged over the finite-sized slabs, results in the initial rapid increase in granular temperature. On the short time scale, inelastic collisions are not the dominant mode of energy dissipation, and therefore the points close to the shock do not collapse. The subsequent slower variation, including the peak value of the granular temperature, occurs over a substantially longer lengthscale. This long term behavior is due to the volume fraction dependent quasi-steady force and the resulting fluctuation in the particle velocity that contributes to granular temperature. It is this latter slower evolution of granular temperature that is of interest here.

The variance of the Voronoi volume fraction is directly tied to the distribution of Voronoi Volumes discussed above. The raw moments of the Voronoi volume fraction can be calculated in terms of the Voronoi volume fraction distribution as

$$\langle \phi_v^n \rangle = \int_0^\infty \left(\frac{V_p}{V_f + \frac{V_p 3\sqrt{2}}{\pi}} \right)^n f(V_f)\ dV_f\,. \tag{39}$$

The moments can be used to calculate variance, skewness, and higher order statistics of the Voronoi volume fraction. Figure 16 shows the Voronoi volume fraction variance for the different coefficients of restitution, where the variance plots are scaled by the initial variance prior to the shock. The figures show the corresponding results for the analytical 3Γ distribution. At each streamwise location, the local mean volume fraction, as given in 17, was used to obtain the corresponding local values of the parameters of the 3Γ distribution. The 3Γ variance increases downstream of the shock and reaches a scaled peak value of 2.00 at a local mean volume fraction of about $\phi = 0.28$. With further increase in local mean volume fraction, the variance of Voronoi volume fraction decreases to a value of about 0.545 for $\phi = 0.55$ in the equilibrium regime. Comparing the result of the elastic limit ($e = 1$) DEM simulation, it can be observed that as with the 3Γ distribution, the variance increases, reaches a peak and decreases to the post-shock equilibrium value. The higher variance values may be attributed to the Voronoi-volume-dependent force fluctuation. The DEM variance of the elastic limit remains higher not only immediately downstream of the shock, but in the equilibrium regime after the particle phase has cooled.

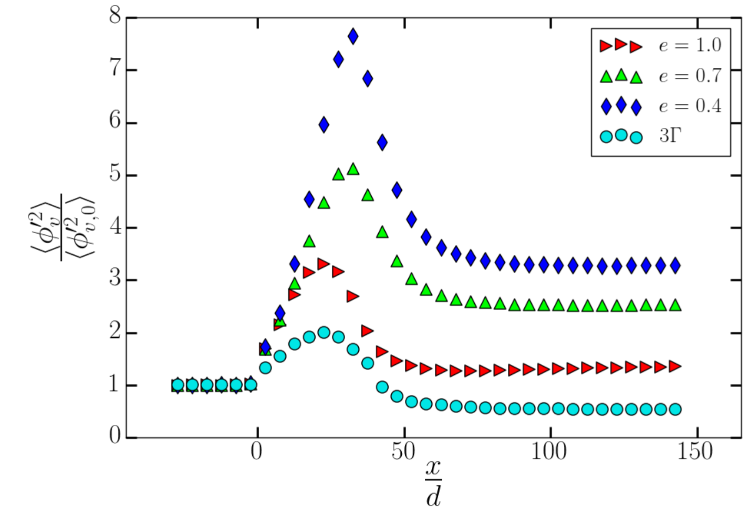

FIG. 16: Case 1: The Voronoi volume fraction variance is plotted for three values of e, as well as the theoretical 3Γ distribution. The variance is scaled by the initial upstream Voronoi variance present in the DEM simulations. For all observed restitution coefficients, the variance first increases for intermediate volume fractions during the compaction of the particles and settles to a lower value in the equilibrium regime. Decreasing the coefficient of restitution is shown to raise the final resting variance.

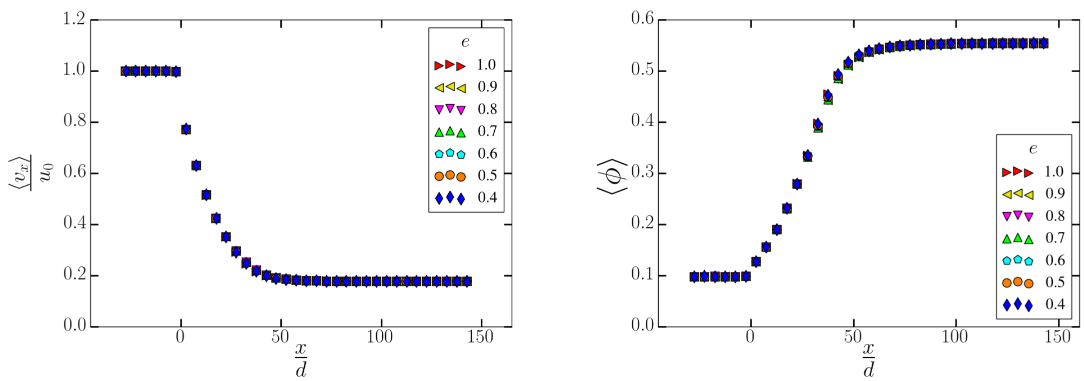

(a) (b)

FIG. 17: Case 1: The ensemble-averaged scaled velocity (a) and the ensemble-averaged volume fraction (b). The coefficient of restitution is shown to have little to no impact upon the mean momentum transfer in the streamwise direction.

As inelasticity is increased, the peak variance in particle volume fraction increases. Though the volume fraction variance decreases following the peak value, the asymptotic post-shock value reached for large x is substantially larger than the value corresponding to the elastic limit and the 3Γ distribution. This clearly suggests that inelastic collisions promote clustering of particles as discussed before. This trend follows classical results obtained for uniform cooling problems in granular flow [19, 27]. If a uniform granular gas is given an initial granular temperature and left to cool, random clusters form, as collisions kill off the fluctuating energy. Particles with close neighbors are the most likely to undergo a collision, where a portion of the random kinetic energy is lost. Post collision, this pair of particles has less random kinetic energy and are thus more likely to remain close together at a higher local volume fraction. This in turn increases the chance of additional particles colliding with the clustered pair, and nucleates the growth of random clustered structures as the granular gas evolves toward a perfectly cooled state. Increased inelasticity, however, appears to slightly slow the rate at which this clustering occurs, as well as the rate at which the gas reaches a cooled state. This can be observed in the fact that the location of peak variance shifts farther away from the shock for inelastic collisions. The elastic limit does not experience cooling due to collision, so the change in Voronoi volume fraction variance must be due to the nonlinear drag force. Thus, the difference between the inelastic coefficients ($e < 1$), and the elastic limit signifies the effect of collisions.

Due to the preferential direction of shock propagation in the x-direction, there is inherent anisotropy in the collisional process and granular temperature. Figure 18 shows the granular temperature in each of the three principle directions as a percentage of the total granular temperature. As the coefficient of restitution is decreased, the anisotropy increases. Opposing trends are seen in the x-temperature compared to the y and z-temperatures. Since the drag force acts primarily in the x-direction, velocity fluctuations in the y and z-direction occur primarily due to collisions. As the coefficient of restitution decreases, collisions dissipate more energy and the granular gas cools more quickly leading to a diminishing temperature contribution in these directions. Since the contributions of all three directions must sum to one, this in turn corresponds to the x-direction holding a larger contribution of the total granular temperature. As with the total granular temperature, a rapid increase before the peak can be observed in the three components as well.

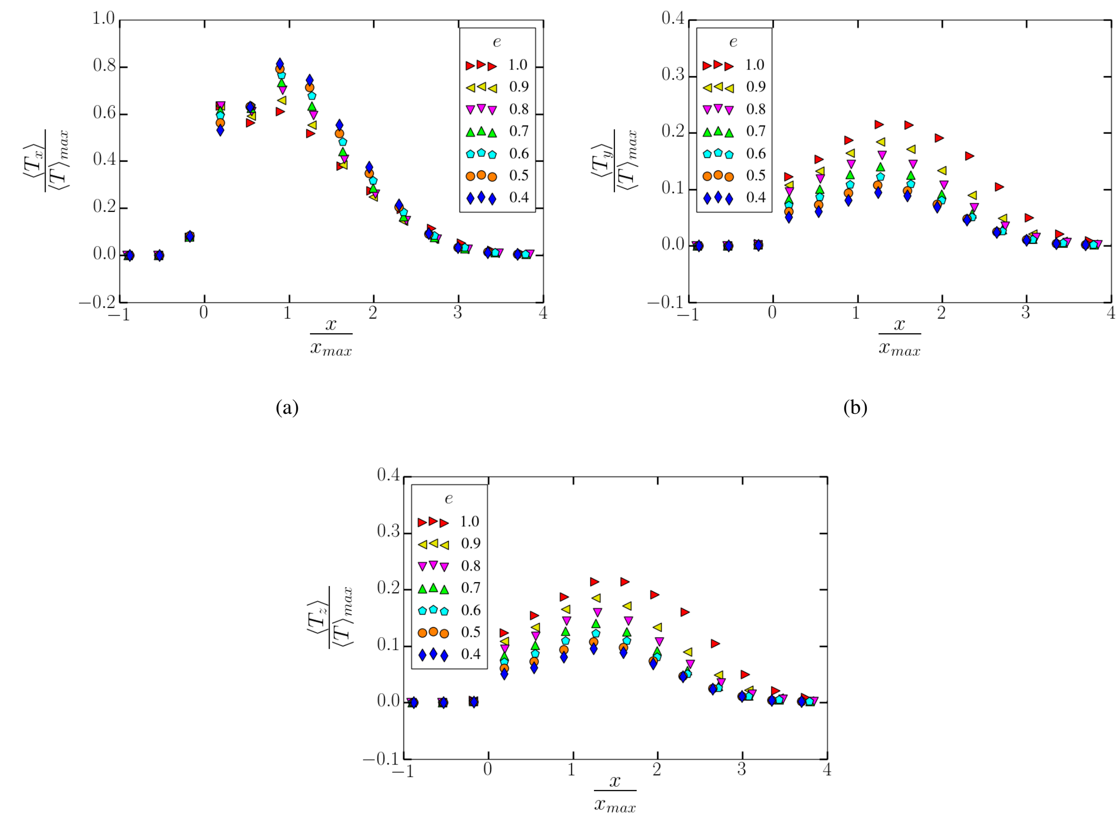

(a)

(b)

(c)

FIG. 18: Case 1: Individual components of the granular temperature are plotted showing that the temperature in the x-direction (a) carries between 56% to 82% of the velocity fluctuations, while the y and z-temperatures (b. and c.) carry 9% to 22% of the velocity fluctuations.

2. *Effect of volume fraction: Case 2* $\phi_0 = 0.05$

Next we investigate a more dilute system where particles enter at an initial volume fraction of $\phi_0 = 0.05$, and compact to an equilibrium volume fraction of $\phi_e = 0.256$. For $\phi_0 = 0.05$, the multiphase shock relations lead to a 5-fold increase in mean volume fraction, as well as a significant velocity jump across the leading shock. Figure 19 shows a plot of the average velocity of the system. This more dilute system takes approximately twice as long to relax to the final equilibrium velocity than that for Case 1, as can be seen by comparing Figures 19 and 17. The increase in relaxation length is expected due to the quasi-steady drag force dependence on the volume fraction. Additionally, the equilibrium fluid to particle density ratio is larger which increases the particle time scale. The effect of this density ratio difference will be discussed further in Case 3.

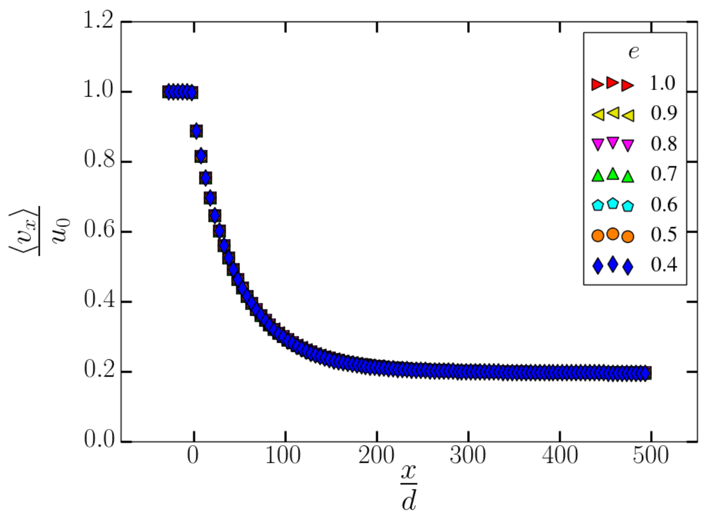

FIG. 19: Case 2: The mean velocity relaxation for $\phi_0 = 0.05$ is shown to be the same for all coefficients of restitution.

Figure 20 shows a plot of the granular temperature scaled by the peak values. The granular temperature exhibits an excellent self-similar collapse for all values of e. The scaled peak values are shown in Figure 21, and are 3 to 4 times smaller than the higher initial volume fraction Case 1, shown in Figure 15 . Like the relaxation length scale, the change in granular temperature profile is expected due to the volume fraction dependence of the quasi-steady force. The Voronoi volume fraction variance in Figure 22 shows that unlike Case 1, the volume fraction variance is monotonically increasing. For the dilute case, at the end of the computational domain at $x = 500d$, the Voronoi volume fraction varies slowly in its approach to the equilibrium state. This trend is seen in the 3Γ distribution plotted in Figure 22. As for Case 1, the elastic limit ($e = 1$) maintains the lowest variance, while the more inelastic cases ($e < 1$) attain a higher variance. Since the equilibrium volume fraction in this case is only 0.256 , we do not observe a decrease in the variance of Voronoi volume fraction as the system is sufficiently far from the close packing limit.

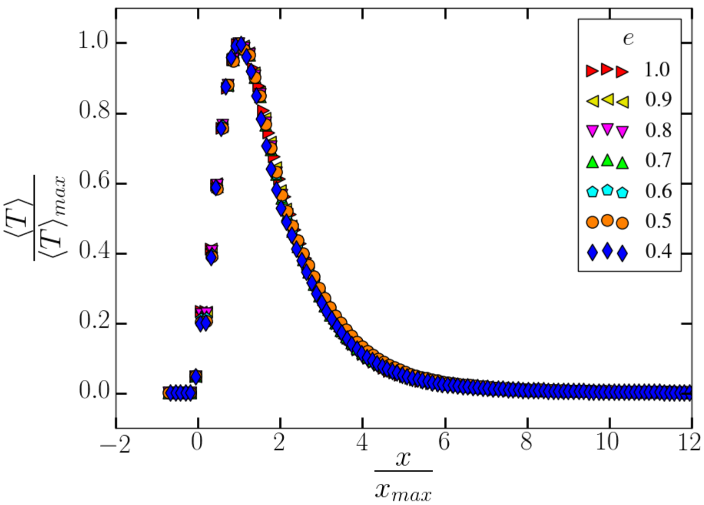

FIG. 20: Case 2: The scaled granular temperature variation is shown for $\phi_0 = 0.05$. Unlike in Case 1, all coefficients of restitutions collapse into a self-similar curve.

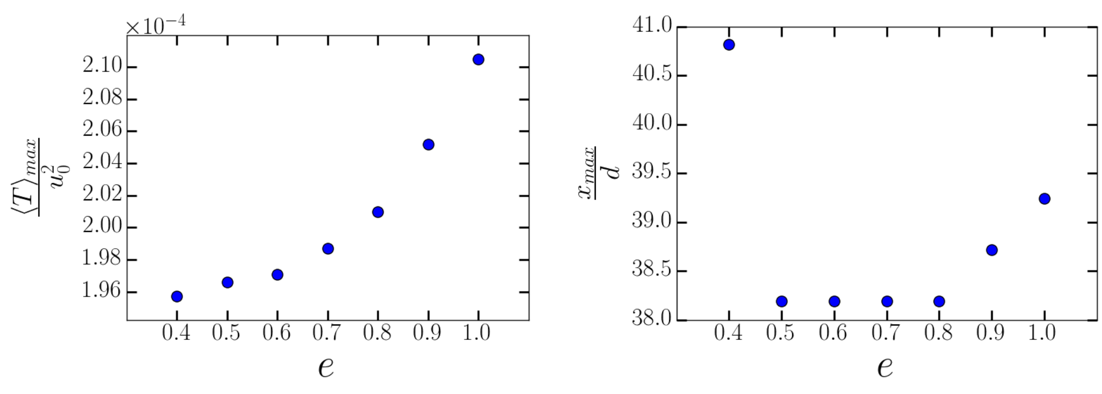

(a) (b)

FIG. 21: Case 2: Peak non-dimensional granular granular temperature (a) and the non-dimensional x-location of the peak (b).

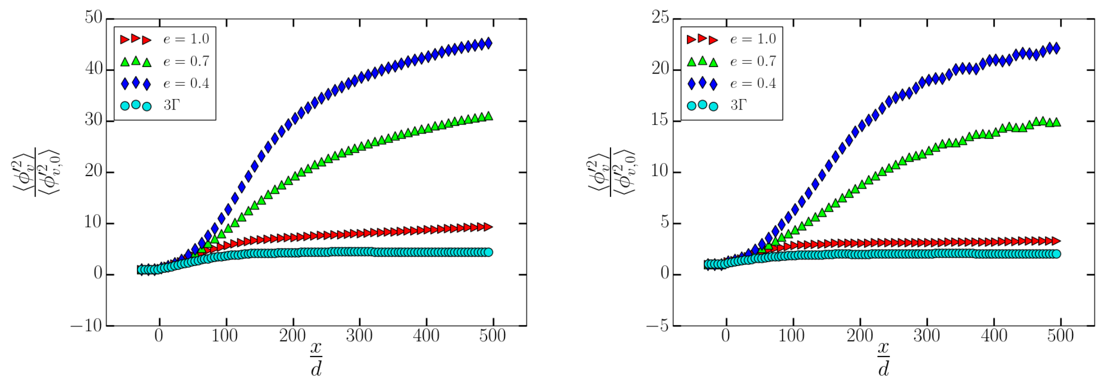

(a)

(b)

FIG. 22: The scaled Voronoi volume fraction variance for $\phi_0 = 0.05$ for Case 2 (a) and Case 3 (b) plotted for 3 values of e as well as the theoretical 3Γ distribution. Unlike in Case 1, the volume fraction variance is monotonically increasing for all values of e as well as the 3Γ distribution.

3. Effect of post-shock density ratio: Case 3, $\delta = 0$

The evolution of the particles downstream of the shock depends primarily on the ratio of the particle density to post-shock equilibrium gas density. Using the multiphase shock relations, an effective way to alter this post-shock equilibrium density ratio is to change the ratio of the specific heat of the particle to the specific heat of the gas (δ). For the case where $\delta = 0$, there is no heat transferred between the gas phase and the particle phase, and the specific heat ratio of the mixture γ_{mix} is equal to the gas γ. Previously in Case 1 with $\delta = 1$, the particle to fluid density ratio was approximately 10. For the Case 3 with $\delta = 0$, this density ratio is raised to approximately 25. Table III shows that the equilibrium velocity for Case 3 is almost twice that of Case 1, and thus the final equilibrium volume fraction is almost half of that of Case 1. While the pressure ratio across the shock does change between Cases 1 and 3, it only changes by about 15 percent. By comparing the multiphase shock properties between Cases 1, 2, and 3, we note that many of the parameters are tightly coupled. Within this framework, it is difficult to study the change of a single parameter in isolation while remaining consistent with the multiphase shock relations.

Due to the density ratio change, as well as the lower equilibrium volume fraction, a longer relaxation length is observed for Case 3 in Figure 23 compared to Cases 1 and 2. The granular temperature has a self-similar collapse, although the peak values of the granular temperature do not follow the trend observed in Cases 1 and 2. Previously, the peak granular temperature increased as the coefficient of restitution was increased. Figure 25, shows that the peak granular temperature slightly decreases as e is increased from a value of $e = 0.4$, and reaches a minimum at an intermediate value of $e = 0.6$, after which the peak granular temperature begins to rise again. Scaled granular temperature plots are shown in Figure 24 for the x and the y-directions (the z-direction is not plotted as it has an identical profile to that of y). The trends for varying coefficient of restitution are consistent with previous results; lowering the coefficient of restitution leads to higher velocity fluctuations in the x-direction, and lower velocity fluctuations in the y and z-directions. The difference in the total granular temperature indicates that the relative size of the streamwise and spanwise velocity fluctuations changes for the different coefficients of restitution. Since the particle time scale, τ_p, is larger in Case 3, the velocity fluctuations in the x-direction do not die off as quickly as they did for Case 1. This leads to a competition between collisional dissipation and aerodynamic drag dissipation. The Voronoi volume fraction variance has a similar profile to the dilute volume fraction case shown in Case 2. Similar to Case 2, the Voronoi variance is monotonically increasing and has not leveled off by the end of the simulation domain.

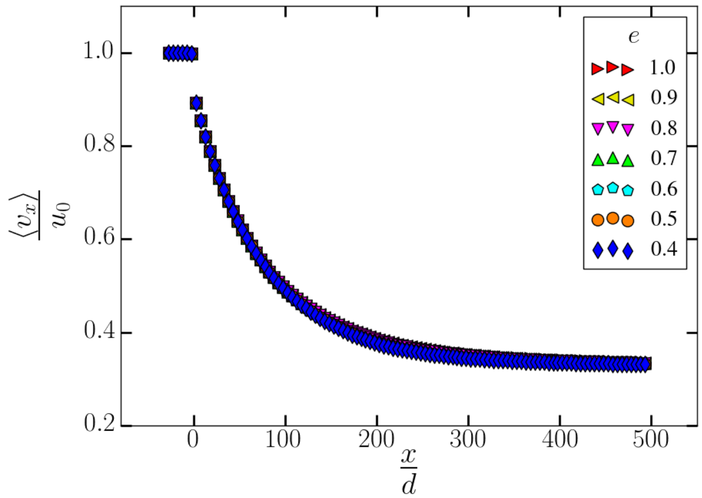

FIG. 23: Case 3: The mean velocity relaxation for $\delta = 0$ is shown to be the same for all coefficients of restitution

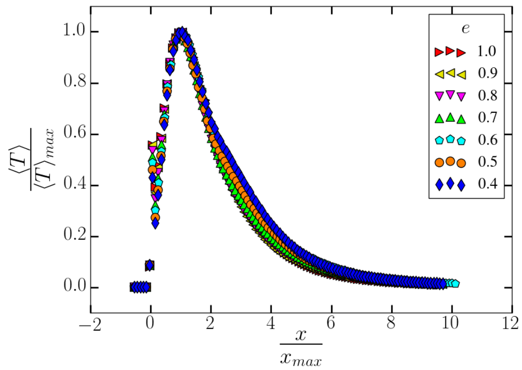

(a)

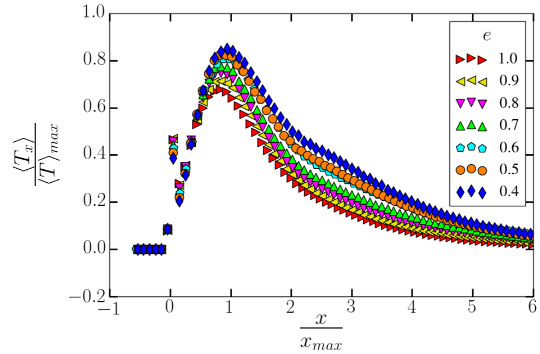

(b)

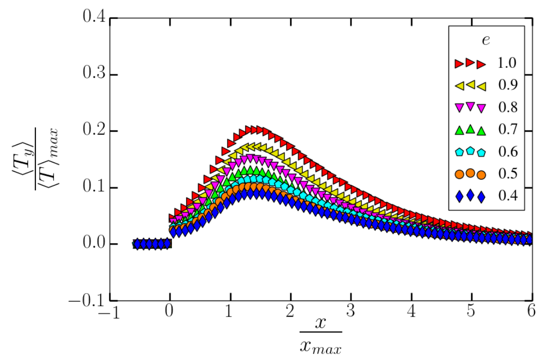

(c)

FIG. 24: Case 3: (a) The scaled granular temperature variation for $\delta = 0$ shows a self-similar collapse under the prescribed scaling. The components of the granular temperature are scaled by the peak total values and plotted for the case where $\delta = 0$. The trends in the x-temperature (b) and the y-temperature (c) are shown to follow that of Case 1 where the relative contributions in the x-direction increase as the coefficient of restitution is lowered while the y-direction contributions increase as the decrease as the coefficient of restitution is lowered.

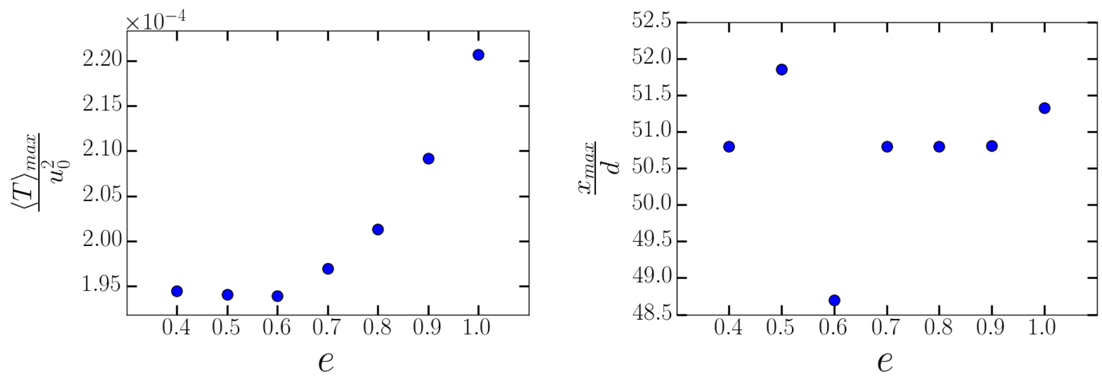

(a)

(b)

FIG. 25: Case 3: For the $\delta = 0$ case the peak granular temperature (a) has an almost parabolic dependence upon e first decreasing and then increasing as e is increased. The location of the peak value (b) follows the trend of Case 1 where it approaches the shock location as the coefficient of restitution is increased.

V. CONCLUSION

The propagation of a planar shock over a bed of particles provides a canonical example to investigate the granular physics of gas-induced particle-particle interaction. This problem nicely complements the classical gravity-driven granular shear flow problem which has been the subject of intense study in the literature. Similar to classical granular shear flow problem, the planar shock problem is statistically stationary. Unlike the granular shear flow problem, however, there is a strong inhomogeneity in the streamwise direction normal to the plane of the shock. One of the key findings of the present investigation is that a random distribution of particles of uniform probability upstream of the shock, develops strong clustering both at the macro and microscales as the shock passes through the bed. Using the Voronoi volume associated with each particle, we observe traveling wave structures that form as the particles pass through the shock, relative to a shock-attached frame of reference. Alternating layers, with substantially higher and lower than the mean particle concentration, are observed to travel downstream at post-shock velocity.

A key aspect of this study is the use of an advanced aerodynamic force model to represent the gas induced force on each particle in terms of quasi-steady, pressure-gradient, and added-mass force contributions. The latter two inviscid forces are significant only during the short period of the shock passing over the particle, as they decay on the acoustic time scale. In contrast, the viscous quasi-steady force acts over a long period until the particle velocity reaches to equilibrium with the post-shock gas velocity. In particular, we model the quasi-steady force to be dependent on local particle volume fraction and this volume fraction dependent drag force has been known to induce instability. This gives rise to macroscale clustering of particles which leads to the observed traveling wave structure in the particle concentration along the inhomogeneous streamwise direction. This particle clustering behavior is observed even in the limit of elastic collisions. With the introduction of inelasticity, through coefficient of restitution $e < 1$, the clustering behavior substantially increases. Inelastic collisions lead to energy dissipation upon each collision and thus promotes clustering of particles at the microscale. This, in combination with the volume fraction dependent drag induced macroscale clustering, leads to large amplitude waviness in the particle concentration downstream of the shock.

The ensemble-averaged statistics for the Voronoi volume fraction upstream of the shock wave show good agreement with a theoretical distribution for randomly distributed particles of uniform probability. However, downstream of the shock wave, the Voronoi volume statistics depart from that of a random distribution, providing a quantitative measure of the clustering behavior. Assuming a synthetic sinusoidal variation in particle volume fraction, we calculated the corresponding theoretical Voronoi volume distribution and showed that it qualitatively describes the distribution observed in the DEM simulations. The variance of the Voronoi volume fraction is seen to increase by orders of magnitude as the inelasticity of the particle collisions is increased. This is an indicator of the intensification of particle clustering due to inelastic collisions. At high volume fractions, the Voronoi volume fraction variance is constrained by the close packing limit. In contrast, dilute systems show a more pronounced clustering behavior.

The granular temperature shows a nearly self-similar collapse when scaled by the peak temperature and the downstream location of the peak. The magnitude of the peak temperature increases as the coefficient of restitution approaches unity. As energy is dissipated due to inelastic collisions, the particle system retains less of its random fluctuating energy resulting in the lower temperature. A majority of the fluctuating energy is stored in the x-direction, which is the direction of the aerodynamic drag force.

The work presented in this paper is greatly simplified by the assumption of the equilibrium gas state immediately downstream of the multiphase shock. Furthermore, we have used the Voronoi volume of the particles to model the gas-mediated force fluctuations that are seen by the particles. Remarkably, these fluctuations form a wave-like clustered particulate structure that follows known instabilities in fluidized beds. Thus, despite the simplifying assumptions, the simulations presented in this paper point to an important particulate structure present in shock-particle interaction problems that future simulations and experiments should be mindful of. Future work should employ more realistic gas dynamics that account for the fully four-way coupled nature of this problem. Additionally, we have demonstrated the use of Voronoi tessellation for both introducing force fluctuations, as well as to quantify clustering of particulate structures.

Appendix A: Appendix

For the case of a planar shock wave passing over a particle, Equation (20) for the inviscid unsteady force can be expressed as assuming the particle velocity to be much smaller than the shock velocity in the laboratory frame

$$\tilde{\boldsymbol{f}}_{iu,i} = \frac{12}{\tilde{\rho}_p} \int_0^{\infty} K_{iu}(\zeta) \Big[\big(\tilde{\rho}_1 \tilde{u}_1 - \tilde{\rho}_0 \tilde{u}_0 \big) \big(\tilde{u}_s(\tau - \zeta) - \frac{1}{2} \big)^2 \tilde{u}_s \Big] d\zeta \;\; \boldsymbol{e}_x \tag{A1}$$

Further, in the limit of a small Mach number, the inviscid Kernel has been explicitly given as

$$K_{iu}(\zeta) = e^{-\zeta} \cos(\zeta) \,. \tag{A2}$$

Plugging the kernel (A2) into (A1) and taking the constant gas properties outside of the integrand, we explicitly evaluate the integral. For the case of a shock passing over a particle, we define τ_a as the non-dimensional arrival time when the shock touches the front of the particle. Till this time (i.e., for $\tau < \tau_a$) the particle is unaware of the shock and therefore $\tilde{\boldsymbol{f}}_{iu,i} = 0$. After the shock arrival time the particle will experience inviscid unsteady force, along with the other force components. We identify two separate time regimes over which the force is active. The first is from τ_a to the time τ_e when the shock reaches the back-end of the particle. During this first regime the shock is located over the particle and the volume-averaged gas properties as seen by the particle change over time. After this time τ_e, the gas properties averaged over the particle is no longer changing, and the inviscid unsteady force is only in response to relative acceleration that happened during $\tau_a \leq \tau \leq \tau_e$. Equation (A2) is broken into the two following integrals.

$$\begin{aligned} \tilde{\boldsymbol{f}}_{iu,i} &= \frac{12}{\tilde{\rho}_p} \tilde{u}_s \big(\tilde{\rho}_1 \tilde{u}_1 - \tilde{\rho}_0 \tilde{u}_0 \big) \int_0^{\tau - \tau_a} e^{-\zeta} \cos(\zeta) \Big(\tilde{u}_s(\tau - \tau_a - \zeta) - \frac{1}{2} \Big)^2 d\zeta \, \boldsymbol{e}_x \;\; \text{for} \;\; \tau_a \leq \tau \leq \tau_e \\ \tilde{\boldsymbol{f}}_{iu,i} &= \frac{12}{\tilde{\rho}_p} \tilde{u}_s \big(\tilde{\rho}_1 \tilde{u}_1 - \tilde{\rho}_0 \tilde{u}_0 \big) \int_{\tau - \tau_e}^{\tau - \tau_a} e^{-\zeta} \cos(\zeta) \Big(\tilde{u}_s(\tau - \tau_a - \zeta) - \frac{1}{2} \Big)^2 d\zeta \, \boldsymbol{e}_x \;\; \text{for} \;\; \tau \geq \tau_e \end{aligned} \tag{A3}$$

We note that the difference between the shock departure and shock arrival time can be approximated as $\tau_b - \tau_a = 1/\tilde{u}_s$ if we ignore the negligible relative motion of the particle during this brief period. Furthermore we shift the time from the shock arrival time to define $\tau' = \tau - \tau_a$. Equation (A3) can be analytically integrated to obtain,

$$\tilde{\boldsymbol{f}}_{iu,i} = \frac{6}{\tilde{\rho}_p}\tilde{u}_s\big(\tilde{\rho}_1\tilde{u}_1 - \tilde{\rho}_0\tilde{u}_0\big)\Big[e^{-\tau'}\sin\tau'\Big(\tilde{u}_s^2 + \tilde{u}_s + \frac{1}{4}\Big) + \Big(e^{-\tau'}\cos\tau' - 1)(\tilde{u}_s^2 - \frac{1}{4}\Big)\Big] \text{ for } \tau' \le \frac{1}{\tilde{u}_s}$$

$$\tilde{\boldsymbol{f}}_{iu,i} = \frac{6}{\tilde{\rho}_p}\tilde{u}_s\big(\tilde{\rho}_1\tilde{u}_1 - \tilde{\rho}_0\tilde{u}_0\big)e^{-\tau'}\Big[\sin\tau'\Big(\tilde{u}_s^2 + \tilde{u}_s + \frac{1}{4}\Big) + \cos\tau'\big(\tilde{u}_s^2 - \frac{1}{4}\big) + e^{\frac{1}{\tilde{u}_s}}\sin\big(\tau' - \frac{1}{\tilde{u}_s}\big)\Big(\tilde{u}_s^2 - \tilde{u}_s + \frac{1}{4}\Big) + \Big(e^{\frac{1}{\tilde{u}_s}}\cos\big(\tau' - \frac{1}{\tilde{u}_s}\big)\Big(\frac{1}{4} - \tilde{u}_s^2\Big)\Big] \text{ for } \tau' \ge \frac{1}{\tilde{u}_s} \tag{A4}$$

---

[1] J. Ai, J.-F. Chen, J. M. Rotter, and J. Y. Ooi. Assessment of rolling resistance models in discrete element simulations. *Powder Technology*, 206(3):269–282, 2011.

[2] G. Akiki, T. Jackson, and S. Balachandar. Force variation within arrays of monodisperse spherical particles. *Physical Review Fluids*, 1(4):044202, 2016.

[3] G. Akiki, T. Jackson, and S. Balachandar. Pairwise interaction extended point-particle model for a random array of monodisperse spheres. *Journal of Fluid Mechanics*, 813:882–928, 2017.

[4] G. Akiki, T. L. Jackson, and S. Balachandar. Pairwise interaction extended point-particle (piep) model for a random array of monodisperse spheres. *Journal of Fluid Mechanics*, 2016 (under review).

[5] S. Annamalai and S. Balachandar. Faxén form of time-domain force on a sphere in unsteady spatially varying viscous compressible flows. *Journal of Fluid Mechanics*, 816:381–411, 2017.

[6] R. Beetstra, M. Van der Hoef, and J. Kuipers. Drag force of intermediate reynolds number flow past mono-and bidisperse arrays of spheres. *AIChE Journal*, 53(2):489–501, 2007.

[7] N. V. Brilliantov, F. Spahn, J.-M. Hertzsch, and T. Pöschel. Model for collisions in granular gases. *Physical review E*, 53(5):5382, 1996.

[8] G. Carrier. Shock waves in a dusty gas. *Journal of Fluid Mechanics*, 4(04):376–382, 1958.

[9] S. Chialvo and S. Sundaresan. A modified kinetic theory for frictional granular flows in dense and diluteregimes. *Physics of Fluids (1994-present)*, 25(7):070603, 2013.

[10] C. T. Crowe, J. D. Schwarzkopf, M. Sommerfeld, and Y. Tsuji. *Multiphase flows with droplets and particles*. CRC press, 2011.

[11] J. S. Curtis and B. Van Wachem. Modeling particle-laden flows: A research outlook. *AIChE Journal*, 50(11):2638–2645, 2004.

[12] A. Di Renzo and F. P. Di Maio. Comparison of contact-force models for the simulation of collisions in dem-based granular flow codes. *Chemical Engineering Science*, 59(3):525–541, 2004.

[13] P. Duru, M. Nicolas, J. Hinch, and E. Guazzelli. Constitutive laws in liquid-fluidized beds. *Journal of Fluid Mechanics*, 452:371–404, 2002.

[14] S. Elghobashi and G. Truesdell. On the two-way interaction between homogeneous turbulence and dispersed solid particles. i: Turbulence modification. *Physics of Fluids A: Fluid Dynamics*, 5(7):1790–1801, 1993.

[15] H. Faxén. Der widerstand gegen die bewegung einer starren kugel in einer zähen flüssigkeit, die zwischen zwei parallelen ebenen wänden eingeschlossen ist. *Annalen der Physik*, 373(10):89–119, 1922.

[16] J.-S. Ferenc and Z. Néda. On the size distribution of poisson voronoi cells. *Physica A: Statistical Mechanics and its Applications*, 385(2):518–526, 2007.

[17] M. García-Villalba, A. G. Kidanemariam, and M. Uhlmann. Dns of vertical plane channel flow with finite-size particles: Voronoi analysis, acceleration statistics and particle-conditioned averaging. *International Journal of Multiphase Flow*, 46:54–74, 2012.

[18] V. Garzó and J. Dufty. Dense fluid transport for inelastic hard spheres. *Physical Review E*, 59(5):5895, 1999.

[19] I. Goldhirsch and G. Zanetti. Clustering instability in dissipative gases. *Physical review letters*, 70(11):1619, 1993.

[20] A. Goldshtein, M. Shapiro, and C. Gutfinger. Mechanics of collisional motion of granular materials. part 3. self-similar shock wave propagation. *Journal of Fluid Mechanics*, 316:29–51, 1996.

[21] Y. Gu, S. Chialvo, and S. Sundaresan. Rheology of cohesive granular materials across multiple dense-flow regimes. *Physical Review E*, 90(3):032206, 2014.

[22] H. Hertz. Über die berührung fester elastischer körper. *Journal für die reine und angewandte Mathematik*, 92:156–171, 1882.

[23] E. A. Lazar, J. K. Mason, R. D. MacPherson, and D. J. Srolovitz. Statistical topology of three-dimensional poisson-voronoi cells and cell boundary networks. *Physical Review E*, 88(6):063309, 2013.

[24] Y. Ling, A. Haselbacher, and S. Balachandar. Importance of unsteady contributions to force and heating for particles in compressible flows: Part 1: Modeling and analysis for shock–particle interaction. *International Journal of Multiphase Flow*, 37(9):1026–1044, 2011.

[25] Y. Ling, A. Haselbacher, and S. Balachandar. Importance of unsteady contributions to force and heating for particles in compressible flows. part 2: Application to particle dispersal by blast waves. *International Journal of Multiphase Flow*, 37(9):1013–1025, 2011.

[26] A. Longhorn. The unsteady, subsonic motion of a sphere in a compressible inviscid fluid. *The Quarterly Journal of Mechanics and Applied Mathematics*, 5(1):64–81, 1952.

[27] S. Luding and H. J. Herrmann. Cluster-growth in freely cooling granular media. *Chaos: An Interdisciplinary Journal of Nonlinear Science*, 9(3):673–681, 1999.

[28] Y. Mehta, C. Neal, T. Jackson, S. Balachandar, and S. Thakur. Propagation of a strong shock over a random bed of spherical particles (accepted). *Journal of Fluid Mechanics*.

[29] R. Monchaux, M. Bourgoin, and A. Cartellier. Preferential concentration of heavy particles: A voronoï analysis. *Physics of Fluids*, 22(10):103304, 2010.

[30] J. Murray. On the mathematics of fluidization part 1. fundamental equations and wave propagation. *Journal of Fluid Mechanics*, 21(3):465–493, 1965.

[31] M. Parmar, A. Haselbacher, and S. Balachandar. Modeling of the unsteady force for shock–particle interaction. *Shock Waves*, 19(4):317–329, 2009.

[32] M. Parmar, A. Haselbacher, and S. Balachandar. Generalized basset-boussinesq-oseen equation for unsteady forces on a sphere in a compressible flow. *Physical review letters*, 106(8):084501, 2011.

[33] M. Parmar, A. Haselbacher, and S. Balachandar. Equation of motion for a sphere in non-uniform compressible flows. *Journal of Fluid Mechanics*, 699:352–375, 2012.

[34] J. Richardson and W. Zaki. The sedimentation of a suspension of uniform spheres under conditions of viscous flow. *Chemical Engineering Science*, 3(2):65–73, 1954.

[35] X. Rogue, G. Rodriguez, J. Haas, and R. Saurel. Experimental and numerical investigation of the shock-induced fluidization of a particles bed. *Shock Waves*, 8(1):29–45, 1998.

[36] P. Rowe. Drag forces in a hydraulic model of a fluidized bed-part ii. *Trans. Inst. Chemical Engineers*, 39:175–180, 1961.

[37] G. Rudinger. Some properties of shock relaxation in gas flows carrying small particles. *Physics of Fluids (1958-1988)*, 7(5):658–663, 1964.

[38] G. Rudinger. Some effects of finite particle volume on the dynamics of gas-particle mixtures. *AIAA journal*, 3(7):1217–1222, 1965.

[39] R. I. Saye and J. A. Sethian. The voronoi implicit interface method for computing multiphase physics. *Proceedings of the National Academy of Sciences*, 108(49):19498–19503, 2011.

[40] T. Schwager and T. Pöschel. Coefficient of restitution and linear–dashpot model revisited. *Granular Matter*, 9(6):465–469, 2007.

[41] V. Senthil Kumar and V. Kumaran. Voronoi cell volume distribution and configurational entropy of hard-spheres. *The Journal of chemical physics*, 123(11):114501, 2005.

[42] L. E. Silbert, D. Ertaş, G. S. Grest, T. C. Halsey, D. Levine, and S. J. Plimpton. Granular flow down an inclined plane: Bagnold scaling and rheology. *Physical Review E*, 64(5):051302, 2001.

[43] M. Sun, T. Saito, K. Takayama, and H. Tanno. Unsteady drag on a sphere by shock wave loading. *Shock waves*, 14(1):3–9, 2005.

[44] M. Tanemura. Statistical distributions of poisson voronoi cells in two and three dimensions. *FORMA-TOKYO-*, 18(4):221–247, 2003.

[45] Y. Tang, E. Peters, J. Kuipers, S. Kriebitzsch, and M. Hoef. A new drag correlation from fully resolved simulations of flow past monodisperse static arrays of spheres. *AIChE journal*, 61(2):688–698, 2015.

[46] S. Tenneti, R. Garg, and S. Subramaniam. Drag law for monodisperse gas–solid systems using particle-resolved direct numerical simulation of flow past fixed assemblies of spheres. *International journal of multiphase flow*, 37(9):1072–1092, 2011.

[47] D. Vescovi, D. Berzi, P. Richard, and N. Brodu. Plane shear flows of frictionless spheres: Kinetic theory and 3d soft-sphere discrete element method simulations. *Physics of Fluids (1994-present)*, 26(5):053305, 2014.

[48] J. L. Wagner, S. J. Beresh, S. P. Kearney, W. M. Trott, J. N. Castaneda, B. O. Pruett, and M. R. Baer. A multiphase shock tube for shock wave interactions with dense particle fields. *Experiments in fluids*, 52(6):1507–1517, 2012.

[49] C. Wen and Y. Yu. Mechanics of fluidization. In *Chem. Eng. Prog. Symp. Ser.*, volume 62, page 100, 1966.

[50] A. A. Zaidi, T. Tsuji, and T. Tanaka. A new relation of drag force for high stokes number monodisperse spheres by direct numerical simulation. *Advanced Powder Technology*, 25(6):1860–1871, 2014.

[51] H. Zhang and H. Makse. Jamming transition in emulsions and granular materials. *Physical Review E*, 72(1):011301, 2005.